Université de Montréal

Test et calibrations technologiques avec PICO-0.1 pour les futurs détecteurs de chambre à bulle de matière sombre de PICO

par

Simon Chen

Département de physique
Faculté des arts et des sciences

Mémoire présenté à la Faculté des études supérieures et postdoctorales
en vue de l'obtention du grade de
Maître ès sciences (M.Sc.)
en physique

août 2020

Sommaire

Parmi les douzaines d'expériences qui visent à découvrir la matière sombre, l'expérience de détection directe PICO utilise des détecteurs à liquide surchauffé comme moyen pour s'y prendre. La chambre à bulle PICO-40L remplie de C_3F_8, présentement située dans le laboratoire sous-terrain SNOLAB, est en cours de test en vue d'une recherche aveugle de WIMP (Weakly Interacting Massive Particle) d'une durée de 1 an. Pour assurer la stabilité du détecteur pendant les périodes de préparation et pendant l'acquisition de données, un logiciel de surveillance a été écrit. Un moyen fiable de surveiller les paramètres importants du détecteur et d'envoyer des alarmes en cas d'urgence joue un rôle important à non seulement au succès de PICO-40L, mais aussi au développement du futur détecteur PICO-500.

Située à l'Université de Montréal, la chambre à bulle PICO-0.1 a été conçue afin de calibrer les nombreux événements de fond qui se présentent dans ce type de détecteur. De plus, cette chambre à bulle a été utilisée comme première tentative au monde de mesurer la diffusion Thomson sur un noyau d'atome en exposant le détecteur rempli de C_3F_8 à une source de gamma produite par la réaction $^{19}F(p,\alpha\gamma)^{16}O$ à l'aide d'un faisceau de protons crée par l'accélérateur de particules de l'Université de Montréal. Ce type d'interaction s'avérera à un événement de fond important pour les expériences de détection directe de matière sombre à bas seuil.

Mots-clés: matière sombre, WIMP, chambre à bulles, PICO, DAQ, diffusion Thomson

Summary

Amongst the dozens of experiments aiming to be the first to claim a dark matter signal, PICO is a direct dark matter detection experiment that utilizes superheated liquid detectors as a means of doing so. The latest C_3F_8 filled PICO-40L bubble chamber currently located in the SNOLAB underground laboratory is under testing to prepare for a 1 live-year blinded WIMP (Weakly Interacting Massive Particle) search. To ensure the stability of the detector during both the testing and the data acquisition phases, a monitoring software was coded. A reliable way to monitor all the parameters and to send alerts accordingly plays an important role in not only the success of PICO-40L, but also the development of the future larger-scale PICO-500 detector.

PICO-0.1 is a test bubble chamber located at the University of Montreal that was built to calibrate for the numerous background events that can occur in this kind of technology. This test chamber was also used as a world's first attempt to measure the coherent (Thomson) photon scattering onto a nucleus by exposing the C_3F_8 filled detector to a gamma source produced by the $^{19}F(p,\alpha\gamma)^{16}O$ reaction using a proton beam created by the University of Montreal particle accelerator. This kind of interaction will prove to be a significant background for future sub-keV direct dark matter detection experiments.

Keywords: dark matter, WIMP, bubble chamber, PICO, DAQ, Thomson scattering

Contents

List of tables

List of figures

Acknowledgements

I'd like to express my gratitude towards both my research supervisors, Viktor Zacek and Alan Robinson, for taking me in as a newly graduated student. To have the patience to work with someone like me, who had little to no experience in this field, you guys have guided in this difficult journey.

Thank you to the PICO collaboration for being not only an amazing group of people to work with but also for pushing the limits of physics and striving to find the needle in the haystack. Keep up the excellent work, it always pays off.

Thank you to everyone that I have met during this academic journey, Mathieu, Deepak, Olivia, François, Frédéric, Émile, Jeremy and Jérémie are only some of the names of the countless people that I have shared laughs, conversations, and concerns with during my stay. You guys have made the trips, the lunches, and the long hours in the bunker worthwhile. A particular thanks to Arthur, an amazing friend that has suffered through my infinite number of questions and my nagging. You've been an inspiration and a role model. Thank you for all the talks we've had, whether they were serious or not.

To all my friends, Carry, Célina, Charlene, Judy, Peter, Ran, Vanessa, and many more, that have brought me up when I was down, lifted me up when times were hard and encouraged me when I needed it, thank you for keeping up with me. I hope I can be half the friend you guys are to me.

Finally, thank you to my family, who has always supported me since the day I was born and encouraged me to pursue anything that interested me, academic or not. I will never be able to pay back for the tremendous love they've given me and the sacrifice they have made to help me get to where I am now.

Introduction

Ever since the first evidence of dark matter in 1933, many theoretical models are proposed to describe this elusive matter. A likely candidate, the WIMP (Weakly Interacting Massive Particle) model suggests that dark matter would only interact at the energy scale of the weak interaction and that these particles would have a mass of up to a couple of TeVs. These kinds of models are pursued by dark matter experiments through different methods such as direct detection, indirect detection, and production with the ultimate goal of recording a dark matter signal within their detectors. As more and more experiments cover larger ranges of dark matter mass and cross section, the current challenge is to increase the sensitivity of future detectors to explore new regions of this parameter space.

The use of superheated liquid detectors is one of the direct detection methods adopted by the PICASSO, COUPP, and the merger between both experiments, PICO collaborations. PICASSO operated multiple detectors with C_4F_{10} droplets spread inside a water-saturated polyacrylamide gel matrix and was able to achieve very good alpha background discrimination through acoustic analysis. On the other hand, COUPP used superheated liquids as a target fluid inside a bubble chamber to be able to measure the recoil of different interactions. The collaboration merger utilized the best of both worlds by adopting excellent alpha discrimination on the newly built PICO-60 bubble chamber.

PICO-40L is the current generation of dark matter detecting bubble chamber filled with C_3F_8 that is being tested at the SNOLAB underground laboratory. This chamber adopts a new "right-side up" design with the idea of mitigating some of the unwanted backgrounds that were present in previous PICO runs while still maintaining its sensitivity. Additionally, this detector will serve as a stepping stone in the development of a much larger bubble chamber, PICO-500.

To calibrate these large scale bubble chambers, the collaboration has built multiple smaller test chambers. PICO-0.1 is a smaller-scale bubble chamber located at Université de Montréal that was previously used to calibrate for different background events. One of the interactions that will slowly dominate the background of sub-keV threshold detectors is the recoil onto the target's nuclei by low energy gammas. PICO-0.1 is used to measure this coherent (Thomson) photon scattering by exposing the detector to a 6.13, 6.92, and 7.12 MeV gamma source produced by the ^{19}F(p,$\alpha\gamma$)^{16}O reaction.

In this thesis, the motivation behind using bubble chambers as a method of WIMP detection will be presented in Chapter 1. Chapter 2 will follow with a presentation of the achievements and results of past PICASSO, COUPP, and PICO detectors. Chapter 3 will describe the newly designed PICO-40L and its attempt to surpass previous dark matter limits.

The final section of this thesis will focus on how PICO-0.1 is used to calibrate for backgrounds and improve the overall sensitivity of this kind of technology. Chapter 5 describes the technicalities of the detector whereas Chapter 6 will present the method and results of a world's first attempt at measuring the coherent (Thomson) photon scattering background using PICO-0.1.

Chapter 1

Dark Matter Detection in Bubble Chambers

1.1. The WIMP Model

The first evidence of dark matter was introduced in 1933 after observations of gravitational effects on the Coma Cluster [**52**]. Ever since, there has been more observational evidence such as galactic rotation curves having a flat velocity distribution along its radius [**42**] and the bending of light through gravitational lensing [**48**] that solidifies proof of the existence of dark matter. In our current understanding of cosmology, dark matter constitutes 23% of the total mass-energy content in the universe whereas ordinary matter only constitutes 5%. The remaining 72% is unknown energy acting on the accelerating expansion of the universe and is called dark energy.

Many theoretical models attempt to pinpoint the expected properties of dark matter based on numerous observed cosmological effects. A candidate must satisfy a couple of conditions: it must be stable on a cosmological time scale, be electrically neutral and have the proper relic density (density at which the abundance of dark matter remained constant). Amongst these models, one likely candidate is the WIMP (Weakly Interacting Massive Particle), which suggests that dark matter would only interact at the energy scale of the weak interaction (weakly interacting) and a mass of 1 GeV to a couple of TeVs (massive particle). One of the compelling arguments in favor of the WIMP is that the expected cross-section of dark matter given its relic density, which was found to be $\simeq 3\times10^{-26}\text{cm}^3\text{s}^{-1}$, is on the same order of magnitude as the weak interaction. This "WIMP miracle" drove many dark matter physicists to explore this region of the cross-section mass parameter space. The current favorite WIMP candidate is the neutralino, the lightest supersymmetric particle that would meet these criteria.

The goal of an experimental dark matter physicist is to measure these theoretical properties and to provide concrete evidence of its interactions. There are three methods of dark matter detection as depicted in Figure 1.1: direct detection, indirect detection, and production. Direct detection experiments such as noble liquid detectors, cryogenic detectors, and superheated liquid bubble chambers aim to measure a low-energy recoil from the interaction of dark matter onto a target nuclei. Indirect detection such as neutrino telescopes looks for self-annihilating dark matter particles outside of Earth that would produce Standard Model particle-antiparticle pairs. A more recent approach to the field of dark matter detection is the production of dark matter particles at particle colliders using proton beams. Although the detectors at the colliders are not able to directly measure its energy since it is not expected to interact with ordinary matter, it can be inferred by looking for missing energy and momentum by comparing the initial and final states of all other detected particles.

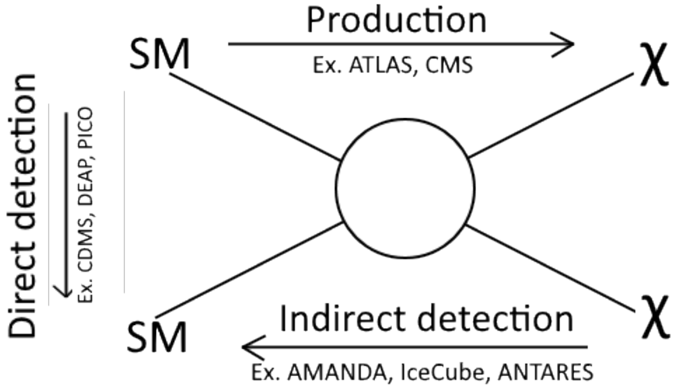

Fig. 1.1. Chart of dark matter detection methods and names of experiments that use the method. SM represents any particle from the Standard Model and χ represents the dark matter particle.

1.1.1. WIMP signal

One of the difficulties in finding a dark matter signal in a direct detection experiment is to recognize a rare WIMP signal amongst a handful of background events. The expected signal can be computed by looking at the recoil rate of the interaction between a WIMP and a nucleus, which is described by the integral over the expected energy spectrum [**35**]:

$$\frac{dR}{dE_{nr}} = \int \frac{1}{E\ r} dR(E) \tag{1.1.1}$$

where $E_{nr} = \frac{\mu^2 v^2}{M_N}(1 - \cos(\theta))$ is the recoil energy at the center of mass, $\mu = \frac{M_N M_\chi}{M_N + M_\chi}$ is the reduced mass of the system, M_N is the mass of the nucleus, M_χ is the WIMP mass, v is the WIMP velocity, θ is the dispersion angle and $r = 4\frac{M_N M_\chi}{(M_N + M_\chi)^2}$. By converting the integral as a function of WIMP velocity instead of energy, the equation 1.1.1 becomes:

$$\frac{dR}{dE_{nr}} = \frac{2\rho_\chi}{M_\chi} \int v f(\vec{v},t) \frac{d\sigma}{dq^2}(q^2,v) d^3v \tag{1.1.2}$$

where ρ_χ is the mass density of dark matter, $f(\vec{v},t)$ is the velocity distribution and $\frac{d\sigma}{dq^2}(q^2,v)$ is the cross section desribed by:

$$\frac{d\sigma}{dq^2}(q^2,v) = \frac{\sigma_0}{4\mu^2 v^2} F^2(q) \tag{1.1.3}$$

where q is the momentum transferred to the nucleus, σ_0 is the cross section at $q = 0$ and $F(q)$ is the nuclear form factor. The properties of the target nuclei used in the detector and the velocity of dark matter with respect to the detector are used to solve the integral. Experiments present their results with the assumption that the velocity distribution of WIMPs follows the Maxwell-Boltzmann velocity distribution, which takes into account the relative velocity of the Earth with respect to the dark matter halo in the galaxy as shown in fig 1.2. However, recent data from the Gaia telescope presented in [**38**] refutes this assumption through evidence of "Dark Shards", which suggests to contain local dark matter velocity streams. This leads to believe that the current results presented by direct dark matter detection experiments in the form of exclusion plots with the dark matter mass on the x-axis and its cross section on the y-axis are based on unphysical assumptions. However, these assumptions are still used as a benchmark to compare different experiments and will also be reviewed once a dark matter signal is claimed.

In addition to the variability in dark matter flux, the spin dependence is also a factor to be considered. Since it is currently unknown whether or not the leading dark matter

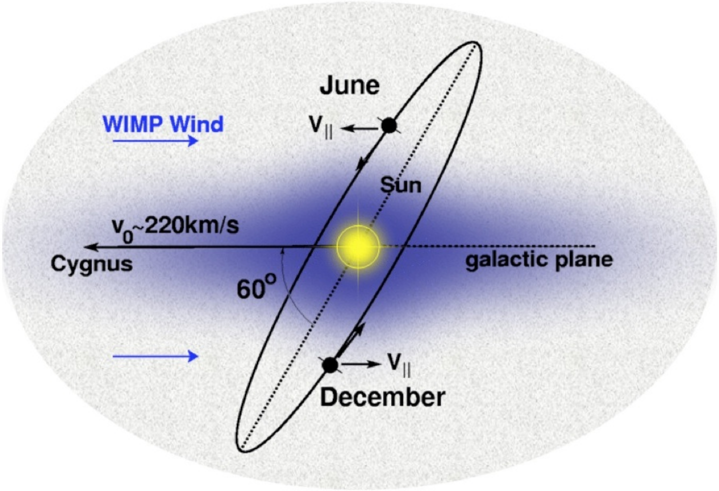

Fig. 1.2. The movement of the Earth inside the dark matter halo in the galaxy creates an effective WIMP wind. The solar system rotates at $v_0 \approx 220$ km/s around the Milky Way and the Earth orbits at a 60° angle around the Sun relative to the galactic plane, resulting in an annual modulation of the WIMP signal. [**37**]

interaction is spin dependent, experiments can cover spin-dependent, spin-independent or both parameter spaces. The sensitivity of spin-independent runs presents itself with limits that are orders of magnitude better than the spin-dependent runs. Figure 1.3 and 1.4 are the current observed and projected results of different experiments.

1.2. Sensitivity of dark matter experiments

The exclusion curves presented previously are explored regions by the detector in which no WIMP event was detected. The sensitivity of these experiments is influenced by two factors: the energy threshold and the background. The former is usually tied to the limitation in the equipment used for the detector and the region of interest explored while the latter is an analysis of all possible external interactions that can occur in the detector.

1.2.1. Background

A background event is all other non-WIMP interactions with the target that can happen inside the detector. Particles such as neutrons, gammas, alphas, and neutrinos can recoil on either the electrons or neutrons and produce a signal that could replicate a dark matter signal. Because the aim of direct detection experiments is to isolate specific WIMP events,

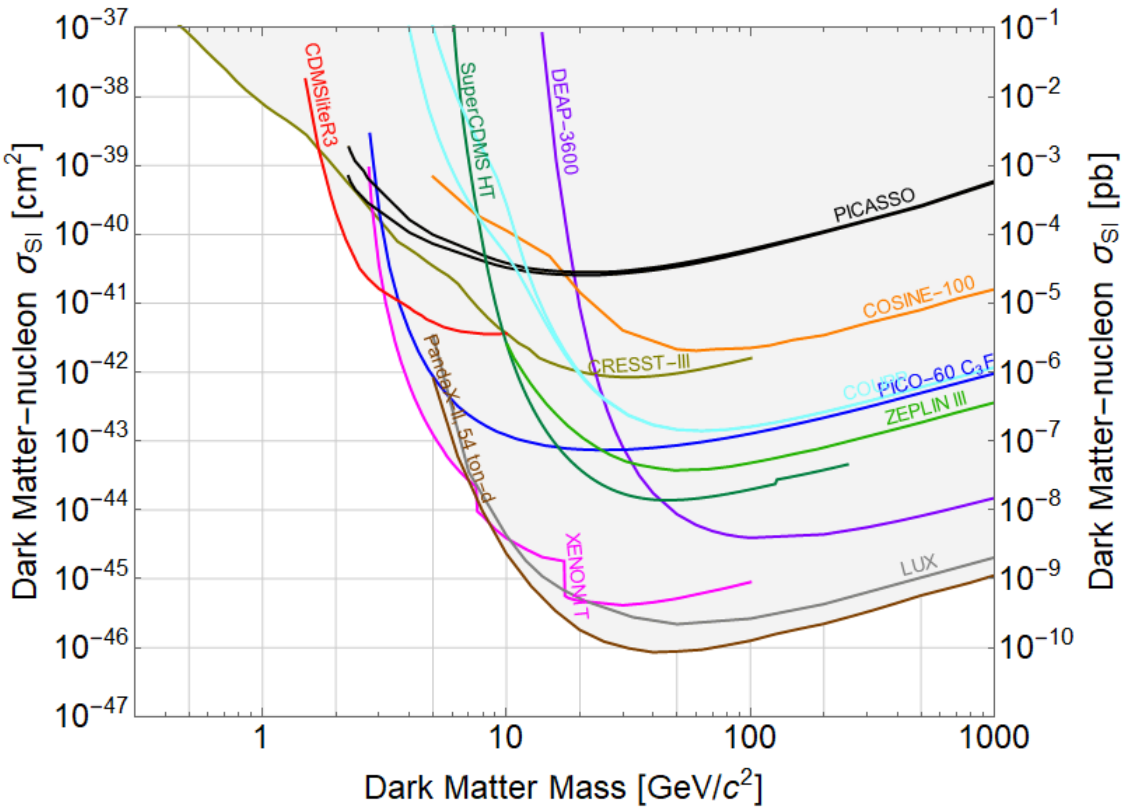

Fig. 1.3. Current spin-independent limit plot created through the SuperCDMS Dark Matter Limit Plotter [**44**]. Results shown for PICASSO (Black [**22**]), LUX (Grey [**8**]), CDMSlite (Red [**6**]), SuperCDMS (Dark Green [**5**]) PandaX (Brown [**25**]), COSINE-100 (Orange [**3**]), CRESST-III (Gold [**2**]), ZEPLIN III (Green [**11**]), COUPP (Cyan [**20**]), PICO-60 (Blue [**16**]), DEAP (Purple [**7**]) and XENON1T (Pink [**19**]). The greyed out region represents the already explored parameter space.

every background must be understood and taken into account in the analysis. Dark matter experiments are sensitive to different kinds of backgrounds based on the characteristics of the detector. Different steps and techniques are used to characterize each contributor. While some experiments are more sensitive to some background events and less sensitive to others, a general background analysis provides an understanding of their contributions.

The first step is to mitigate as many background events as possible through the use of physical improvements to the detector such as shielding, the use of material with the least radiation and running the experiment in a controlled environment. As an example, the liquid argon experiment, DEAP, uses a water tank as a means of shielding against neutrons

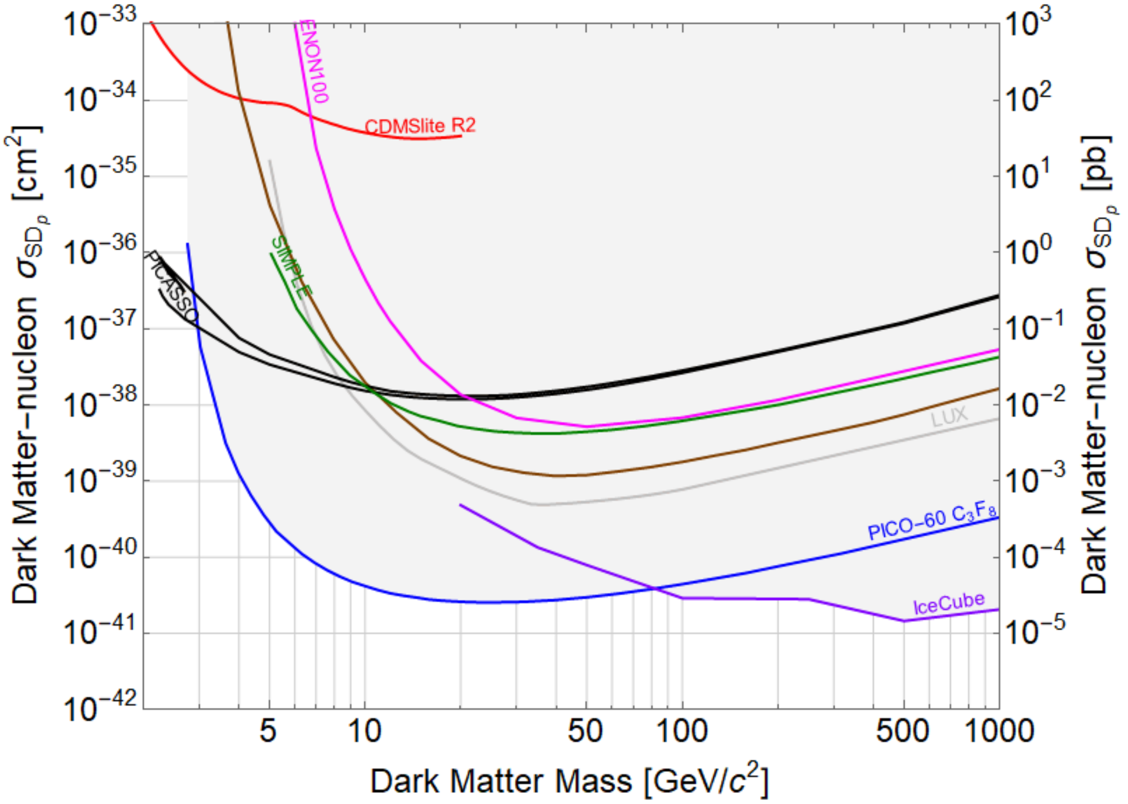

Fig. 1.4. Current spin-dependent WIMP-proton limit plot created through the SuperCDMS Dark Matter Limit Plotter [**44**]. Results shown for PICASSO (Black [**22**]), LUX (Grey [**9**]), CDMSlite (Red [**4**]), PandaX-II (Brown [**29**]), SIMPLE (Green [**27**]), PICO-60 (Blue [**16**]), IceCube (Purple [**1**] and XENON100 (Pink [**18**]). The greyed out region represents the already explored parameter space.

and gammas and operates in SNOLAB, an underground laboratory, to protect itself against cosmic rays [**34**]. A conceptual design of DEAP-50T shows a 44 feet diameter water tank bathing the detector depicted in Figure 1.5.

Afterward, certain specific signals from incoming particles that are completely different from the expected WIMP signal can be discriminated depending on the detector. Since particles interact differently with an electron as opposed to a neutron, discrimination must be made to properly identify the signal for each background. For example, the PICO experiment measures the acoustic power of an event to discriminate between alpha decays and nuclear recoil, which will be further explain in Chapter 2. Finally, for direct background contributions within the WIMP search region of interest, calibrations are made by the main detector or by

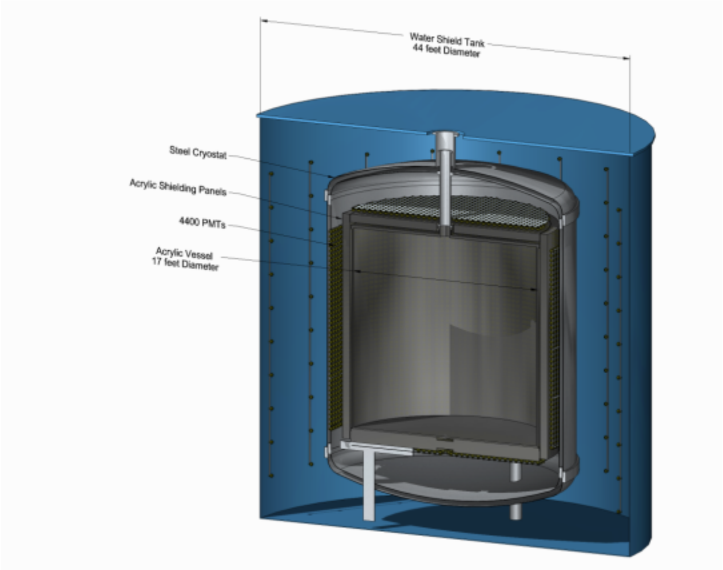

Fig. 1.5. Concept design of DEAP-50T, a 50 tonnes liquid argon detector that uses water for background shielding. [**32**]

secondary prototypes of the detector. After measuring the desired background, simulations are performed to compare the data. The final background analysis results are typically presented as a count rate or an expected contribution to the main data set that follows a Poisson distribution with a 90% confidence interval. Thorough background analysis and control within the region of interest can significantly improve the sensitivity of detection methods and would allow isolation of targeted WIMP events.

1.3. Coherent neutrino-nucleus scattering

One of the backgrounds to direct dark matter experiments are neutrinos that elastically scatter off the nucleus, in a process called coherent elastic neutrino-nucleus scattering (CEvNS). This process occurs when a neutrino interacts with a nucleus via the exchange of a Z boson and produces a recoil. This was first theorized in 1974 [**28**] but measured in 2017 by the COHERENT experiment using a CsI[NA] crystal detector at the neutrino producing Spallation Neutron Source (SNS) [**10**]. The cross section of this neutrino-nucleus interaction is enhanced due to the coherence of this process and is proportional to N^2, the square of the number of neutrons in the target nucleus. However, despite its high interaction cross section, it can only be measured at a very low energy threshold. For current dark matter experiments, the sensitivity of the detectors does not reach this threshold yet but will be reached in future generations of detectors. Figure 1.6 shows the CEvNS background in relation to the current limits on dark matter experiments.

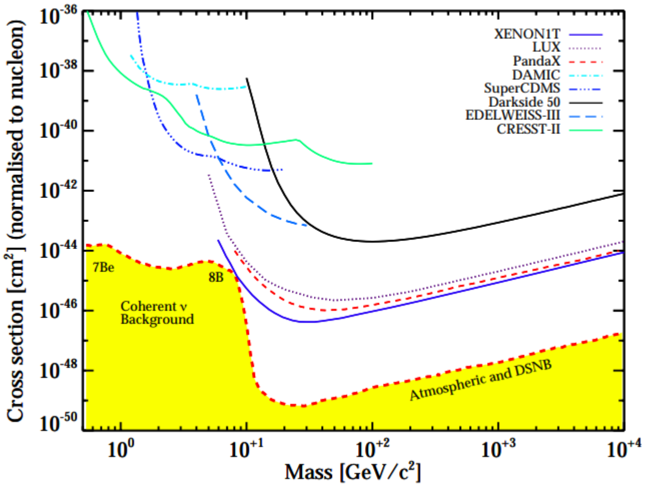

Fig. 1.6. Exclusion plot for spin-independent direct dark matter detection experiments showcasing the neutrino floor that will dominate the background (yellow).

Once detectors reach this "neutrino floor" in sensitivity, the background will be dominated by CEvNS due to the abundant solar neutrino flux. Since this small recoil signal replicates that expected of a WIMP signal, it will be nearly impossible to distinguish them. Moving forward, experiments will have to either find a way to characterize and discriminate these events or conceive a detector insensitive to neutrinos.

1.4. Bubble Chambers and the Seitz Model

The bubble chamber is one of the technologies used for particle detection. It was first used to measure the track of a charged particle [**30**]. Similar to the cloud chamber, which detects the particle's track by observing ionized droplets in a supersaturated vapor chamber [**50**], the bubble chamber detects the particle through the vaporization of a superheated liquid. A modern bubble chamber detector consists of a cylindrical jar with a target superheated liquid and a regulating pressure system. It detects incoming particles by having the target liquid in a metastable state at a temperature and pressure slightly below its boiling point. The incoming particle would deposit energy and would vaporize the liquid and create a bubble. By measuring the energy deposition and examining the way the bubble is formed, it can be inferred what particle caused this change of state. When energy is deposited onto the superheated liquid due to an incoming particle, a heat spike triggers a local phase transition and creates a bubble. This bubble can either shrink and collapse on itself or expand macroscopically. The condition for a bubble of critical radius r_c of to form and expand is:

$$r_c > \frac{2\sigma}{P_b - P_l} \tag{1.4.1}$$

where σ is the surface tension of the bubble and $P_b - P_l$ is the difference in pressure between the bubble and the liquid. The Seitz Theory suggests that the heat spike produced by the radiation of the target fluid inside this critical radius will have a critical energy E_c:

$$E_c = 4\pi r_c^2(\sigma - T\frac{\partial\sigma}{\partial T}) + \frac{4\pi}{3}r_c^3\rho_b(h_b - h_l) - \frac{4\pi}{3}r_c^3(P_b - P_l) + \mathcal{O}(\frac{\delta}{r_c}) \tag{1.4.2}$$

where, T is the temperature, ρ_b is the bubble's density and $h_b - h_l$ is the difference in enthalpies between the bubble and the liquid. The first term represents the energy required to form the surface of the bubble inside a thermal reservoir, the second term is the energy required to vaporize the liquid to form the interior of the bubble, the third term is the mechanical work done on the expansion of the bubble. The critical energy translates to the energy threshold at which the detector operates and is determined by the temperature and pressure conditions set on the detector. Figure 1.7 shows the threshold for C_3F_8 as a function of pressure for different fixed temperatures. Dark matter detecting experiments, such as PICO, are conceived to go as low as possible in energy thresholds to be able to detect the slightest recoil due to a dark matter interaction. These experiments must also avoid detecting non-dark matter interactions which are generally substantial at lower energy thresholds.

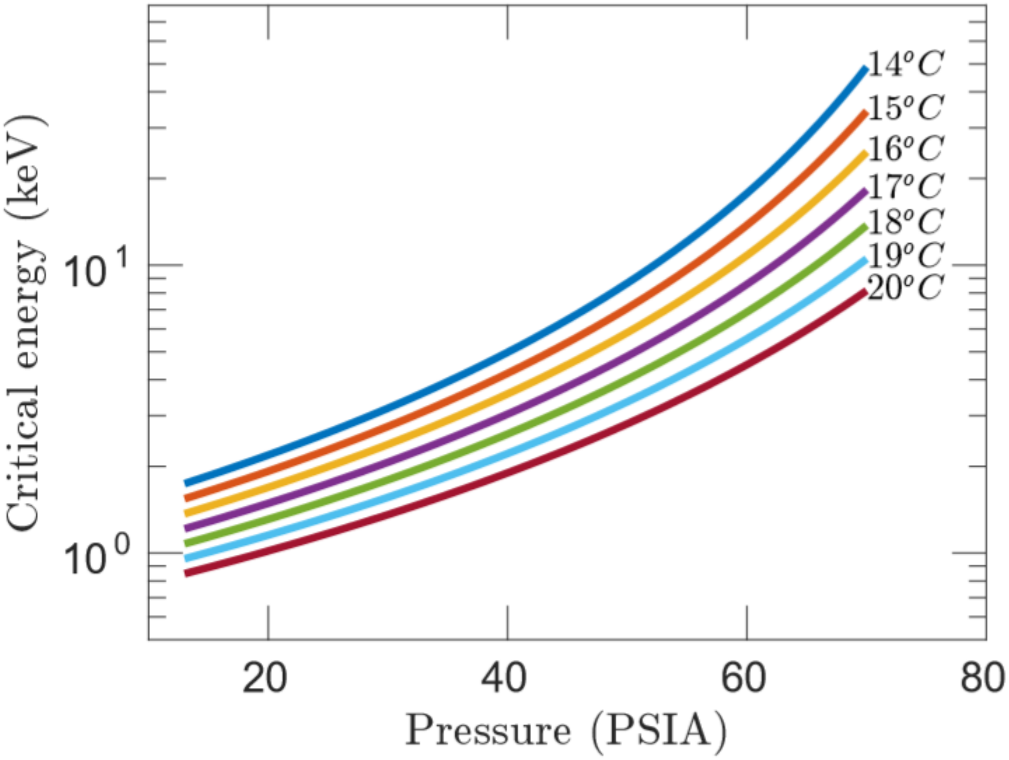

Fig. 1.7. Critical energy (Seitz Threshold) required for bubble nucleation as a function of the pressure at different temperatures for C_3F_8 [**39**].

Chapter 2

The PICO Experiment

The development of superheated fluid detectors has evolved rapidly in the last decade. The PICO collaboration is a result of a merger between two previous collaborations: PICASSO (**P**roject **I**n **CA**nada to **S**earch for **S**upersymmetric **O**bjects) and COUPP (**C**hicagoland **O**bservatory for **U**nderground **P**article **P**hysics). Both collaborations specialized in superheated liquid fluid detectors: PICASSO developed superheated droplet detector whereas COUPP used bubble chambers. Bubbles nucleated from the decay of alpha particles, which is one of the major backgrounds for this type of technology, were partially discriminated by an acoustic analysis technique found by PICASSO. It was then applied to COUPP 4kg and, following the merger of both experiments, PICO detectors. PICO-60 was the first bubble chamber commissioned by the merged PICO experiment and utilized the strengths of both predecessors. An unknown background, caused by the interaction of water and particulates during the runs, was present in PICO-60 and PICO-2L, which lead to the development of a new "right-side up" design for the future PICO-40L.

The PICASSO, COUPP and PICO experiments operated their detectors in SNOLAB, an underground clean laboratory located in Sudbury, Ontario, Canada. The depth of 2km provides invaluable shielding against cosmic rays for the neutrino and dark matter experiment it houses with a muon flux of less than 0.27 $\mu/\mathrm{m}^2/\mathrm{day}$ [**45**]. It is the second deepest underground laboratory in the world next to the 2.4 km deep China Jinping Underground Laboratory [**51**].

2.1. PICASSO

The PICASSO experiment, which ran until 2014, used a superheated liquid droplet technique in their bubble chamber to detect WIMPs described in [**22**]. Droplets of perfluorobutane (C_4F_{10}) with a diameter of around 200 μm were dispersed inside 32 jars of water-saturated polyacrylamide. Each module from the latest generation was 17 cm in diameter and 40 cm in height and contained an active mass of approximately 90g of C_4F_{10}. An example of one of the modules is depicted in Figure 2.1 (a). Each of the jars were topped off with mineral oil and a hydraulic manifold for pressure control and placed inside a thermally and acoustically insulated pressure unit in groups of 4, shown in Figure 2.1 (b).

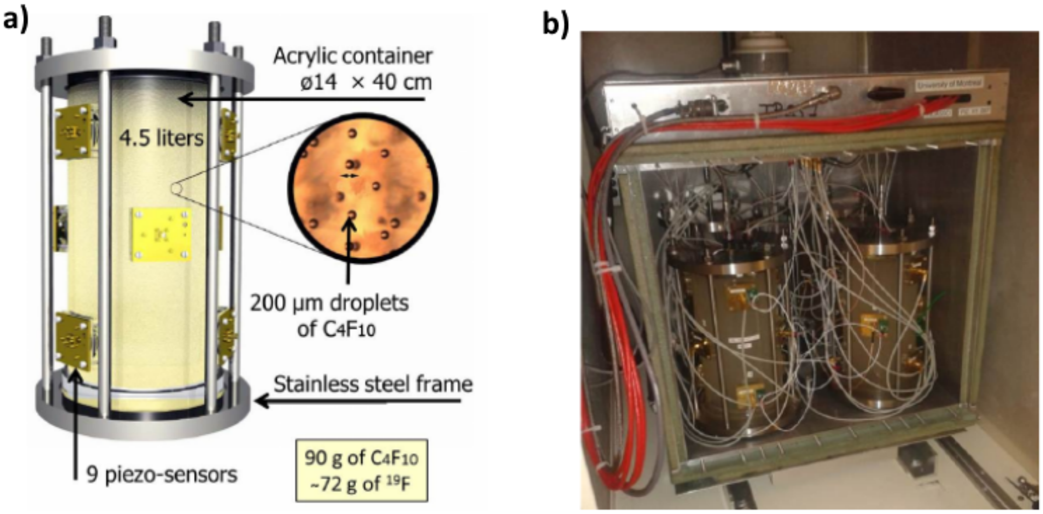

Fig. 2.1. **a**: Single PICASSO module filled with water-saturated polyacrylamide and C_4F_{10} droplets. **b**: Thermally and acoustically insulated pressure unit housing 4 modules.

2.1.1. Detection technique

The detection technique follows one of a bubble chamber described in Section 1.4: the controlled temperature and pressure environment set the energy threshold for the phase transition of the superheated C_4F_{10} droplets to occur. Once an interacting particle deposits the necessary critical energy E_c onto one of the droplets, it vaporizes and emits an acoustic signal captured by the piezos attached to the side of each module. Each WIMP run would have a livetime of around 40 to 50 hours and is followed by a compression phase of 12 hours to reduce the droplet back to its original state while preventing over-expansion and damage to the gel matrix. The livetime of a run is defined as the total duration during which the detector is live and actively recording data.

2.1.2. Analysis and results

To discriminate the background acoustic signals, external sources such as neutron beams and fast neutron sources were used to calibrate and characterize the waveforms of particle-induced signals. The dataset goes through a series of cuts and corrections due to electronic noise, mechanical disturbances, unexpected mystery events along the edges, etc. The final results of PICASSO's 231.4 kg-day exposure between March 2012 and January 2014 showed no indication of a WIMP signal in both the spin-independent and spin-dependent sectors with limits of 4.9×10^{-5} pb at $M_W = 7$ GeV/c^2 and 1.32×10^{-2} pb at $M_W = 20$ GeV/c^2 respectively at a 90% confidence limit as shown in Figure 1.3 and 1.4. However, the latest results showed to have significant improvements to the previous 2012 results due to the addition of better cuts and more data and also proved to have the best spin-dependent limit at low thresholds of around 2-5 GeV/c^2. The alpha background discrimination technique developed by the PICASSO experiment through the analysis of acoustic signals proved to be monumental to the future of bubble chamber since alpha events represent a large portion of the background for this technology.

2.2. COUPP

The COUPP experiment developed bubble chambers. Deployed to SNOLAB in 2010, using the alpha discrimination developed by PICASSO, the COUPP-4kg detector was a fused silica bell jar with 150mm in diameter and supporting stainless steel bellows for pressure control inside a pressure vessel filled with propylene glycol [**21**]. The jar encapsulated 4.0 kg of liquid CF_3I as a target fluid to their dark matter search and uses two cameras attached to the pressure vessel to record bubble events inside the detector. Four piezoelectric transducers were attached to the top of the jar to record the acoustic emission from the bubble formation to discriminate background events.

2.2.1. Detection technique

As a threshold detector, the thermodynamic conditions reflect the sensitivity at which the system operates as described by the Seitz Theory. The detector starts in a compressed state at around 215 PSIA and ramps down to an expanded state of 30.1 PSIA in 5 seconds to bring the fluid below the vapour pressure, then a pressure stabilization period of 30 seconds ensures that the detector is at the right pressure for data taking. Following this period, the detector either triggers due to an event or times out after 500 seconds, re-compressing the system. The trigger occurs when the recoil energy deposited on the target fluid by an incoming particle is above the operating threshold energy of the detector, a bubble forms and triggers the cameras to record a frame by frame sequence of images and the piezos record the acoustics of the event. Figure 2.2 shows an image of a bubble event in the bubble chamber.

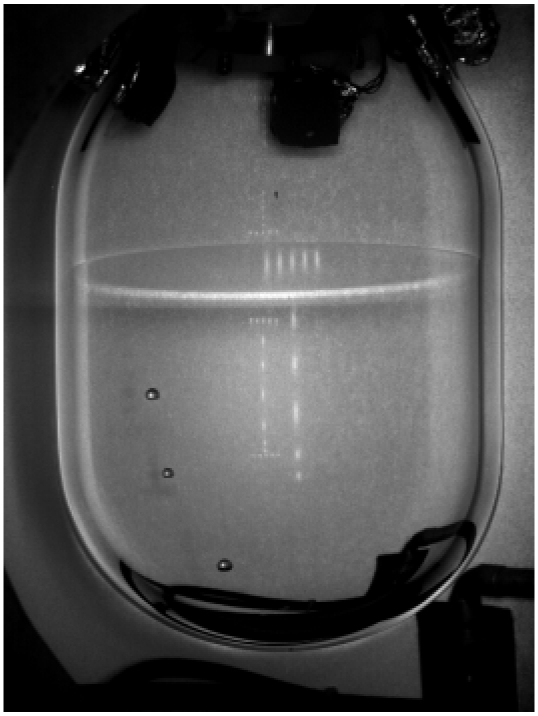

Fig. 2.2. Example of a bubble event captured by the cameras in the COUPP-4kg run. The faint halo line indicates the separation between the target fluid (bottom) and the water buffer (top). The piezos can also be seen attached on top of the jar.

2.2.2. Analysis and results

The data analysis consisted of three steps: image analysis to determine the number of bubbles and spatial position of the bubbles, pressure rise analysis to identify bubbles near the walls and acoustic analysis to classify the type of event. The neutron background events were simulated considering the composition of the material surrounding the detector and the gamma efficiency was measured by placing sources inside the water tank. The results presented by COUPP 4kg 553.0 kg-day exposure between November 2010 to June 2011 at thresholds of 7.8 ± 1.1, 11.0 ± 1.6 and 15.5 ± 2.3 keV showed 20 candidate single nuclear recoil events and 3 multiple bubble events, up from the predicted 5.3 single nuclear recoil events and 2.2 multiple bubble events. Despite these events passing the imposed cuts, these events were found to be dependent on previous expansions, which lead to the presence of unknown background events. Considering the 20 dark matter candidates, the 90% confidence limit of this result is shown in Figure 1.3 for spin-independent WIMPs and Figure 1.4 for spin-dependent WIMPs. Despite this remaining background, the high alpha even rate in COUPP-4kg provided the best demonstration of the efficiency of alpha acoustic discrimination to date of >99.2%.

2.3. Previous PICO detectors

2.3.1. PICO-60 (CF_3I)

Initially developed as COUPP-60, this project, along with PICO-2L, were first major projects of the merged PICO collaboration. This experiment featured a larger scale bubble chamber containing 36.8 kg of CF_3I as opposed to the COUPP-4kg run in Section 2.2 [**13**]. The detector setup was a scaled-up version of the previous COUPP-4kg detector as shown in Figure 2.3, a fused silica jar containing the target fluid supported by bellows inside a pressure vessel.

The 1335 kg-day exposure after cuts of this run at a continuum of thresholds between 7 keV and 20 keV found 0 dark matter candidates and 1 multiple bubble event, which consistent with the predicted 1 single bubble nuclear recoil event and 1 multiple bubble event. However, a significant number of unexpected background events were found in the low acoustic power region shown in Figure 2.4. Although these events were distinguishable from a dark matter signal, the lack of understanding of their origin would prove difficult to the future of bubble chamber detectors.

2.3.2. PICO-2L (Run 1)

The PICO-2L detector featured a 2 liters bubble chamber described in [**12**]. The setup of the experiment was similar to the COUPP-4kg: a fused silica bell jar of the same size,

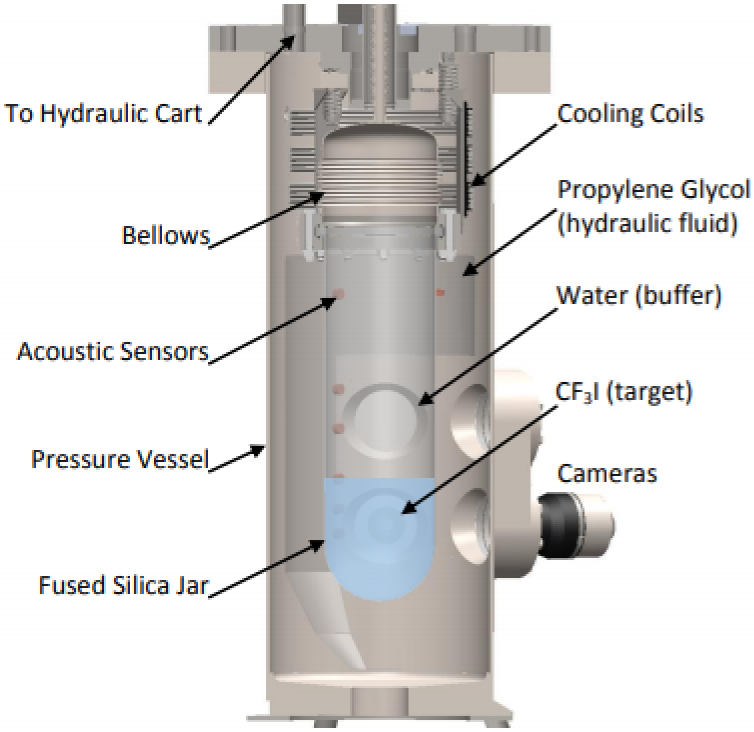

Fig. 2.3. Schematic of the PICO-60 detector.

mounted piezos, stainless steel bellows, and a pressure vessel, as shown in Figure 2.5. The primary goal of the experiment was to compare using C_3F_8 as a target fluid as opposed to CF_3I to see whether or not the unknown events were still present. To do so, the jar was filled with 2.90 kg of C_3F_8 and the background efficiency was measured with the help of calibrations and simulations.

Improvements to the measurable neutron background were made to the surrounding materials of the detector such as the piezos, which contains less radioactivity than previous ones. Also, the AP was found to be dependent on alpha energy using C_3F_8, which allowed an improved acoustic cut on the data. The first WIMP search of this detector ran at thresholds of 3.2, 4.4, 6.1 and 8.1 keV with a total exposure of 211.5 kg-day with more exposure at the 3.2 and 6.1 keV threshold. This WIMP search yielded 9 candidates at 3.2 keV and 3 candidates at 6.1 keV. However, the same unknown background present in the CF_3I run was also seen in this run. Further investigation suggested that these events originated from particulates merging with the water in the buffer creating a point-initiated bubble with acoustic emission within the AP range of the WIMP search. Surface properties of the active fluid, buffer liquid

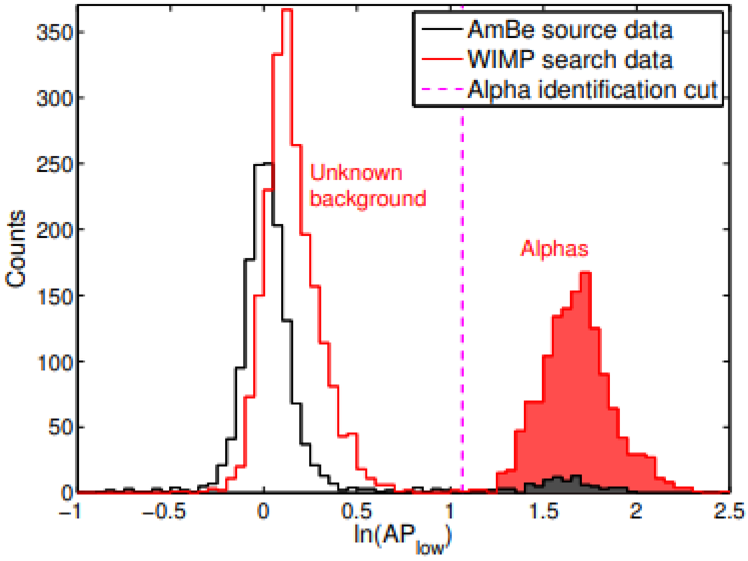

Fig. 2.4. AP distribution between 7 and 64 kHz of PICO-60 CF_3I run with neutron calibration data (black) and WIMP search data (red). An excess of unknown background events can be seen. This background was later found to be caused by the interaction between water and particulates.

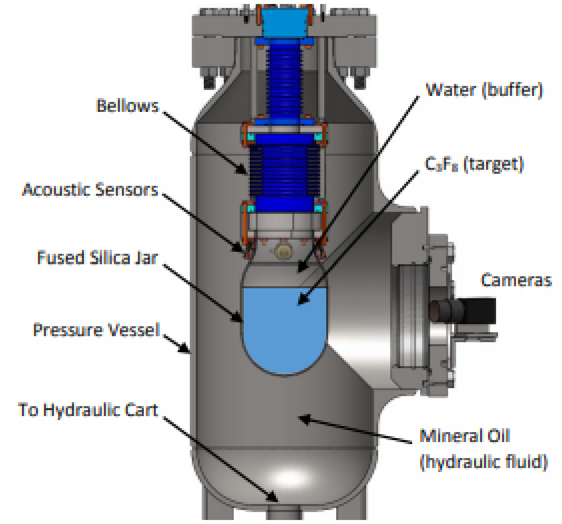

Fig. 2.5. Schematic of the PICO-2L detector.

and jar can influence the bubble formation conditions at the interface and create excess events at the surface. These particulates can originate from external contamination, metal fatigue from the stainless steel bellows, and stress fracturing from silica. Although these events can be cut during the analysis, it greatly reduces the livetime of the run. To avoid this background, it was suggested to either use another buffer fluid such as linear alkylbenzene. [**40**]

2.3.3. PICO-2L (Run 2)

The second run of PICO-2L tested whether careful cleaning and reduced particulate production could reduce the observed background rate. This includes the use of a fused silica flange as opposed to the quartz flange which lowered the radioactivity of particulates, leading to a lower background. In addition, significant attention was devoted to the cleanliness of the detector during the reassembly to ensure maximum mitigation of the expected particulate background. The second run was at a threshold of 3.3 keV with an exposure of 129 kg-day and observed 1 single bubble nuclear recoil event and 3 multiple bubble events [**14**]. This result was consistent with the predicted number of nuclear recoil events from radioactive backgrounds and concluded that the unknown background from previous runs was removed. The results are presented in Figure 1.3 for the spin-independent WIMP and Figure 1.4 for the spin-dependent WIMP.

In addition to the world-leading limits achieved by the detector at the time, PICO-2L brought invaluable information to the future of bubble chambers in search of dark matter. The operating threshold of the bubble chamber was able to achieve lower thresholds than previously capable, able to correct for the unknown background that was present in CF_3I runs and reinforce a thorough cleaning procedure to avoid the particulates in future runs.

2.3.4. PICO-60 (C_3F_8)

Concurrent with PICO-2L run 2, PICO-60 was rebuilt with a significantly modified design, fluid, and assembly procedure. Following the C_3F_8 tests with the PICO-2L chamber, the PICO-60 detector shown in Figure 2.3 was recommissioned with 52.2 kg of C_3F_8 as a target fluid instead of CF_3I [**15**]. In order to avoid the particulate contamination found previously, every component was cleaned and assembled at a military level standard MIL-STD-1246C level 50 before closing the inner volume [**24**]. Improvements to the setup include a new low-stress seal design between the bellows and the jar, additional cameras and a new chiller for better temperature stability in the water tank. The first run at a threshold of 3.3 keV with an exposure of 1167 kg-day found 0 single bubble nuclear recoil WIMP candidates and 3 multiple bubble vents, which was consistent with the predicted 0.24 ± 0.09 single bubble nuclear recoil events and 0.96 ± 0.34 multiple bubble events. In addition, it was noticed that the bubble rate for this run was lower than the previous run with the improved cleaning technique which helped reduce the number of particulate background events.

Following this run, the pressure and temperature limits were pushed to explore lower thresholds. The detector was able to achieve a stable nucleation threshold of 1.81 keV. At this level, increasing sensitivity to gammas in the environment would cause electron recoil events in the bubble chamber to dominate the background. The threshold for the second exposure was set at 2.45 keV, where the neutron background rate would be similar to the 3.3 keV run. With an exposure of 1404 kg-day, 3 single bubble nuclear recoil events and 2 multiple bubble events were recorded after the cuts, consistent with the expected neutron background. Before the decommissioning of PICO-60, a stable threshold of 1.20 keV was achieved with the expected electron recoil background to dominate.

The PICO experiment is currently commissioning a new bubble chamber design with the aim of having better efficiency and limits to other current dark matter experiments. The collaboration opted for a new "right-side up" design which attempts to further eliminate the particulate problem present in previous detectors through the removal of a buffer fluid. A detailed presentation of this detector will be presented in the following chapter. A summary of the running conditions of all previous PICASSO, COUPP, and PICO runs before PICO-40L are presented in Table 2.1.

	PICASSO	COUPP 4kg	PICO-60 (CF_3I)	PICO-2L (Run 1)	PICO-2L (Run 2)	PICO-60 (C_3F_8)
Target fluid	C_4F_{10}	CF_3I	CF_3I	C_3F_8	C_3F_8	C_3F_8
Threshold (keV)	1 to 40	7.8, 11.0, 15.5	7 to 20	3.2, 4.4, 6.1, 8.1	3.3	3.3, 2.45
Exposure (kg-day)	231.4	553	1335	211.5	129	1167, 1404
Number of Single (Multiple) Bubble Events	0	20 (3)	0 (1)	12 (0)	1 (3)	0 (3), 3(2)

Tab. 2.1. Summary of all dark matter detecting bubble chambers in the PICO collaboration prior to PICO-40L.

Chapter 3

PICO-40L

During PICO-60's operations, some of the collaboration's efforts were invested into the research and development of the next generation of bubble chamber for direct dark matter detection, PICO-40L. PICO-40L does not follow the design of the previous PICO and COUPP detectors shown in Figure 2.3, instead the experiment opted for a right-side up type detector as shown in Figure 3.1 (left). This completely new design aims to eliminate the use of a water buffer as a piston, which was the cause of background events in previous PICO runs. This design must be tested in order to move forward and apply it to the next generation of PICO detectors, PICO-500.

3.1. Right-Side Up Design

The new right-side up design aimed to fix some problems that was present in previous detectors. As explained in Section 2.3.2, an unknown background caused by water particulates inside the detector created an abnormally large number of unexplained background events. Although a strict cleaning procedure was imposed to avoid this, the omission of the water buffer would completely eliminate such issue. With this new design, the water buffer previously used a piston for the pressure system was replaced by a fused silica piston with a temperature gradient. Another problem the old design had was, depending on the thermodynamic conditions of the detector, the target fluid (C_3F_8) could condense while the detector was either expanded or compressed. This led to the possibility of the fluid entering the bellows and seal regions, and either becoming trapped, cavitating on surfaces, and/or stirring and transporting particulates down towards the active region. By flipping the detector right-side up, bubbles rise away from the bellows and metal particulates fall away from

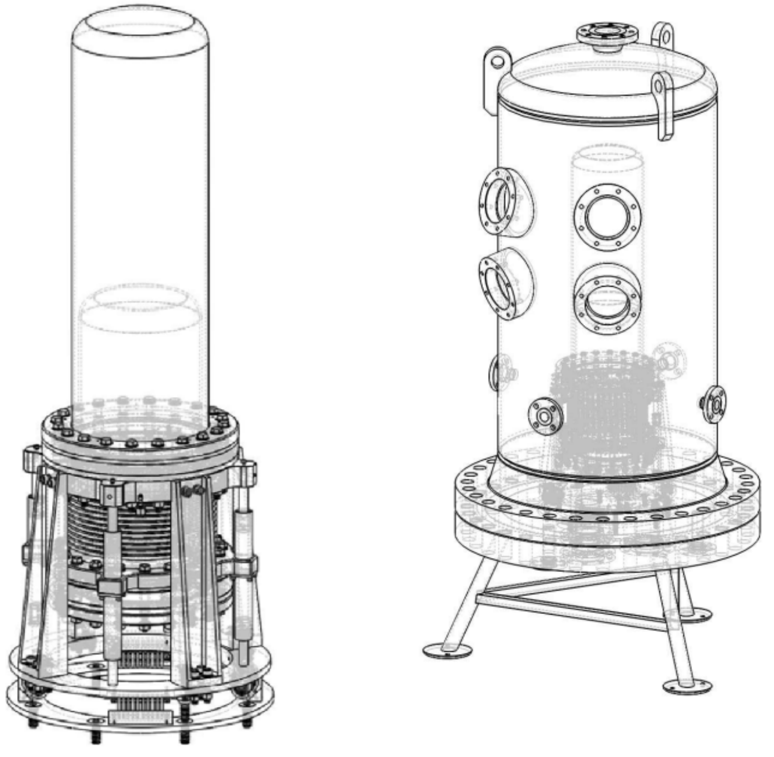

Fig. 3.1. Left: Concept design of the PICO-40L right-side up detector. **Right:** PICO-40L detector inside the pressure vessel.

the active region. Finally, the surface tension between the water and the target fluid was a source of background reducing detector livetime. By avoiding all non-silica interfaces in the warm region, the surface tension between two liquids is no longer present.

The detector is composed of a outer silica jar with a height of 1001mm, an inner radius of 145mm, and a volume of 64.44L and an inner silica jar with a height of 673mm, an inner radius of 131mm and a volume of 35.07L on top of a bellow system for pressure control [**33**]. Multiple sensors for pressure (pressure transducers) and temperature (resistance temperature detectors) are attached to components of the detector to monitor their states and to record the operating conditions during the analysis. The detector itself is placed inside a stainless steel pressure vessel with a radius of 457mm with a top shell and a bottom flange of approximately 2.59m in length, as shown in Figure 3.1 (right).

3.2. Detector Stability

One of the key parts of running a successful direct dark matter detector is to ensure that the detector itself is as stable as possible to be able to maximize the livetime during the WIMP search. For the PICO bubble chambers, this means minimizing any possible downtime such as expansion time, compression time, and event rate. Figure 3.2 shows an example of an event cycle for a PICO bubble chamber.

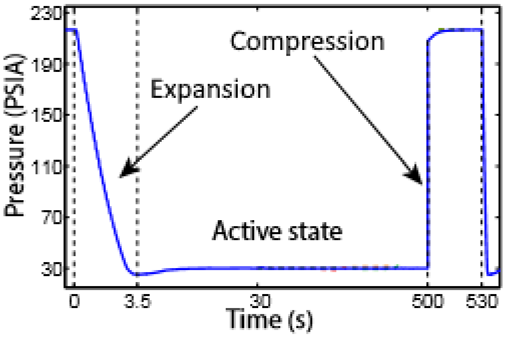

Fig. 3.2. Example of a typical PICO bubble chamber cycle. Pressures and times are for reference only and can vary from one detector run to another. Before an event, the detector starts in a compressed state and expands in a couple of seconds to reach the pressure setpoint where the detector stays until either an event causes a trigger or a set timeout (500 seconds in this case) is reached. There is a compression cooldown time (30 seconds in this case) after every trigger.

3.2.1. Expansion and Compression Time

Getting the expansion and compression time as low as possible through hardware and software optimization is crucial to maximize the detector's livetime. The expansion time aims to be as short as possible relies heavily on the hardware and the responsiveness of the optimized software to reach the proper pressure set point. A necessary compression time is required to be able to run the detector. Once a bubble event occurs, the compression of the detector causes the bubble to collapse, which creates a local heat spike. A cooldown time is required to reach thermal equilibrium around the collapsed bubble before being able to expand for the next event.

3.2.2. Event rate

Another way to gain as much livetime as possible is to reduce the event rate of the detector since fewer events directly translate to less expansion and compression times. Other than WIMP events and background events (explained in Section 3.4), sources of excessive nucleation (hearafter called instabilities) of the detector can create unwanted events that hinder its normal operation. In previous PICO detectors, this includes events caused by particulates (Section 2.3.2), wall and interface events caused by surface tension and dissolved gas contamination, and convective currents in the fluid due to large volumes. Although the new PICO-40L design can help prevent some of these events, lack of experience with the design necessitates the reevaluation of all potential causes of instability. Thorough testing of this detector before the WIMP search is crucial to the success of the experiment. One of the important works of this thesis presented in Chapter 4 is the creation of a clear monitoring interface to be able to pinpoint exactly where stability issues may occur.

3.3. PICO-40L Run Plan

The PICO-40L detector is currently built and being tested for stability. The sensitivity of the detector relies heavily on the capacity of the temperature and pressure components to maintain its operating conditions without failure. Following all testing, the detector is expected to start a blinded WIMP search run of 1 live-year filled with 56kg of C_3F_8 at a threshold of 2.8 keV. A blind run is used to prevent an experiment's results to be biased, which can be unintentionally intended if an experiment sets its cuts after seeing the results. In PICO's case, the information of the bubble events is not revealed until after the unblinding, where variable cuts and the expected background analysis are already set. The blind analysis makes the results provided by the experiment more reliable.

3.4. Backgrounds in PICO-40L

As a direct detection experiment, the most important part of the experiment is to properly mitigate and evaluate every possible background event. For the PICO-40L bubble chamber, this means any non-WIMP interaction that can create a bubble inside the jar during operations. As previously mentioned, the bubble nucleation process requires a minimal recoil energy for the macroscopic expansion of a bubble and usually follows the Seitz Theory in

Section 1.4. For background events that cannot be shielded against, an estimation based on calibrations and simulations are made.

3.4.1. Nuclear recoils

A nuclear recoil can occur whenever a particle with enough energy and momentum to scatter off a neutron inside the detector. This is the most important background to take into consideration as it can mimic the expected WIMP-nucleon scattering produced by dark matter. Both neutrons and neutrinos can produce a background event, but since neutrinos have a relatively low interaction cross-section, explained in Section 3.4.4, neutrons are the main source of this background.

In the construction phase of the detector, this background is minimized as much as possible by evaluating against the radioactivity of optimal components that were assayed. Some sources such as ^{238}U and ^{238}Th, that are present in important detector components like piezos and retroreflector, can spontaneously fission and produce neutrons that interact with the bubble chamber. In addition, (α, n) reactions from ambient interactions can also create a nuclear recoil. A water bath surrounding the pressure vessel shown in Figure 3.3 blocks ambient neutrons coming from the lab. To estimate the contribution of each radioactive component in the experiment setup during the run, GEANT4 simulations evaluate the impact of each of the sources based on their given geometry.

One well-established behaviour of neutrons from past experiments and external calibrations is the bubble multiplicity of an event. Unlike the expected WIMP-nucleon interactions, neutrons are more likely to produce more than one bubble along their track per event, which allows straightforward discrimination between neutron events and WIMP events. Simulations expect that the background due to neutrons from (α, n) and spontaneous fission will produce up to 3 times more multiple bubble events than single bubble events.

3.4.2. Electron recoils

One of the large advantages of superheated liquid bubble chambers is its low sensitivity to gammas in the operating conditions for our dark matter search. The gamma nucleation probability increases drastically as the detector becomes more sensitive with a lower threshold. To evaluate the sensitivity of PICO detectors towards background gammas, external

	Component Leakage prob. S(M) × 10^4	Singles/year × 10^4	Multiples/year × 10^4
OV quartz jar	729 (1857)	0.0095 ± 0.0056	0.024 ± 0.014
IV quartz jar	126 (279)	0.0011 ± 0.0007	0.0025 ± 0.0015
Bellows	0.049 (0.099)	74 ± 17	151.2 ± 34.6
Titanium	0.15 (0.32)	5.4 ± 5.5	11.3 ± 11.5
Piezos	34 (71)	54 ± 79	113 ± 166
Piezos (PICO-84)	54 (111)	7055 ± 2909	14619 ± 6023
Heating 99(261)	99 (261)	939 ± 958	2255 ± 2300
Retro reflector	0.26 (0.70)	2.2 ± 0.7	6.1 ± 2.0
Camera	0.07 (0.19)	9.4 ± 2.0	25.3 ± 5.3
Lenses	0.06 (0.18)	98 ± 23	287 ± 66
PCB & LEDs	0.07 (0.18)	3.4 ± 1.4	9.1 ± 3.8
Pressure Vessel	0.03 (0.09)	358 ± 82	992 ± 226
Oil	41 (106)	57534 ± 56917	147038 ± 145439
Plastic thermal shield	0.007 (0.014)	0.93 ± 0.25	1.9 ± 0.48

Tab. 3.1. Table of simulation results from neutron recoil events of various PICO-40L components using GEANT4 by Arthur Plante [**39**]. The leakage probability of each component for single (multiple) events is based on the geometry of the simulation itself while the singles/year and multiples/year indicate the simulated expected event rate per year for single bubble events and multiple bubble events.

radioactive sources are exposed to the jar and the nucleation probability as a function of threshold energy is recorded.

Although the nucleation process of electron recoils in CF_3I roughly followed the hot-spike nucleation model through the release of heat described by the Seitz Model, gamma calibration data from tests chambers show that this model failed to describe the nucleation process for jars filled with C_3F_8. In [**17**], a fit was performed on over 20 independent calibration data from C_3F_8 filled bubble chambers using multiple sources and found that the bubble nucleation process occurs by ionization rather than by heat.

Fig. 3.3. PICO-40L detector in SNOLAB during its final installation phase. The filled C_3F_8 jar is inside the pressure vessel, which is placed inside a tank to be closed up and filled with water as a shielding against backgrounds.

3.4.3. Alpha recoils

Alpha particles from the decay of radioactive elements, such as radon and polonium, produce a background inside the detector. These events are minimized by using components that contain the least amount of these elements and by taking precaution during any step of the assembly to prevent any external contamination. Before the assembly, material used for PICO-40L are scanned for radioactive content and evaluated appropriately.

However, alpha events can be discriminated through the analysis of their acoustic signal. The acoustic power classifies the signal read from the piezos, corrected for the position of the bubble, in frequency bands. This method of distinguishing between an alpha and a neutron recoil was initially implemented in PICASSO bubble chambers. Calibration data from PICASSO shown in Figure 3.4 show a clear discrepancy in acoustic power between alpha dominated signals and neutron dominated signals.

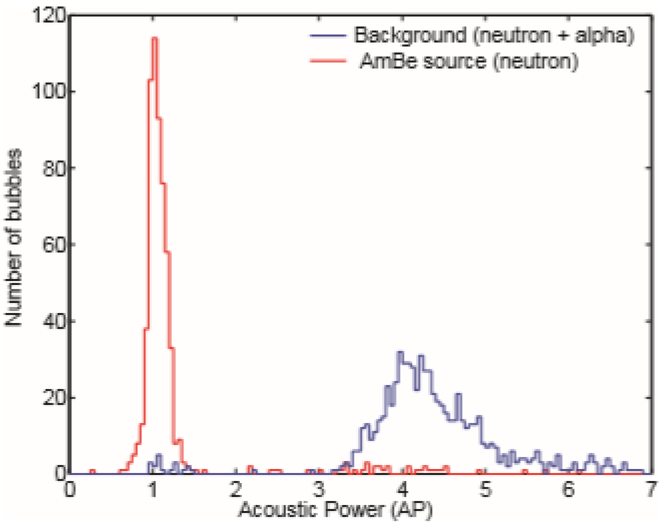

Fig. 3.4. Alpha recoil calibration from the COUPP-4kg experiment [**21**]. The number of bubbles as a function of the acoustic power for background data (blue) and for neutron calibration data (red).

The ability to distinguish both signals based on the acoustic power makes it so that alpha background does not affect the WIMP signal analysis, which means that the primary goal is to minimize the number of alpha events in order to maximize the detector livetime of other possible WIMP signals.

3.4.4. Cosmic rays

Depending on the thermodynamic conditions of the system, low energy interactions will not trigger the detector due to its inability to create a bubble. The Earth receives a large neutrino flux and can cause background in the detector. However, since the interaction cross-section for neutrinos is relatively low with respect to the conditions at which PICO-40L will be running at, the number of neutrino events during the WIMP search was found to be 1.3 events per year based on simulations and the expected neutrino flux.

Cosmic muons are also a possible source of background for PICO-40L. Fortunately, the detector is heavily shielded against them due to the 2 km rock overburded provided by the location of the lab, which estimates that the muon flux to be less than 0.27 $\mu/\mathrm{m}^2/\mathrm{day}$. One way muons interact with the detector is by scattering off electrons. However, due to the low sensitivity of PICO-40L towards electron recoils, the background rate of these muons are insignificant. One of the important contributions caused by muons are the ones that induce neutrons, which are thought to be produced by the interaction between muons and underground rocks.

Chapter 4

Data Acquisition Software

A data acquisition system (DAQ) is crucial for any experiment and is used to collect information about the physical condition of the experiment. Traditionally, physically writing the numerical value of the data produced by an experiment can be a way of data acquisition. This is done for instance to log the operating parameters of University of Montreal's Tandem accelerator (Section 6.1). However, with modern experiments, the success of the experiment can heavily rely on the frequency at which the data is recorded. To optimize this process, the use of a computerized system can automatically collect the data. It does so by converting any signal produced by a sensor to a digital readable signal. Generally, sensors will produce an electrical signal that will be translated through the internal circuit which results in a digital readout. For the case of PICO-40L, a data acquisition system must be implemented to be able to record and monitor important parameters such as temperatures and pressures at very high frequencies (from hundreds to thousands times per second). However, to be able to achieve this automation, a lot of internal programming is required.

One of the programs required for data monitoring is the slow DAQ, an external program that has the capacity of remotely reading and recording parameters from the main DAQ. Monitoring the conditions of the detector at all times is crucial to the success of the experiment especially during the WIMP search since an operator is not always present at the physical detector to correct any failures. In addition, a monitoring database allows a preliminary analysis of the data during the run to ensure that nothing is going wrong. The conception of the slow DAQ user interface program is one of the significant projects from this thesis is presented in the following sections of this chapter.

4.1. Front end of the SlowDAQ Monitoring UI

The monitoring user interface (UI) is a program within the PICO-40L servers that is remotely accessible through Virtual Network Computing (VNC). Instructions on accessing the slow DAQ is found on the PICO docdb entry 4659. The goal of the program is to ultimately be able to monitor and change certain parameters of the PICO-40L detector. It features four tabs: an overview tab, a hydraulic system tab, a temperature system tab, and a water system tab.

4.1.1. Overview

The overview tab displays the important detector parameters from the other three tabs and summarizes it into a general tab as shown in Figure 4.1. However, features such as plotting and trigger are only seen in this tab. A distinctive colored background replicating the actual detector reflects the approximate real position of multiple sensors.

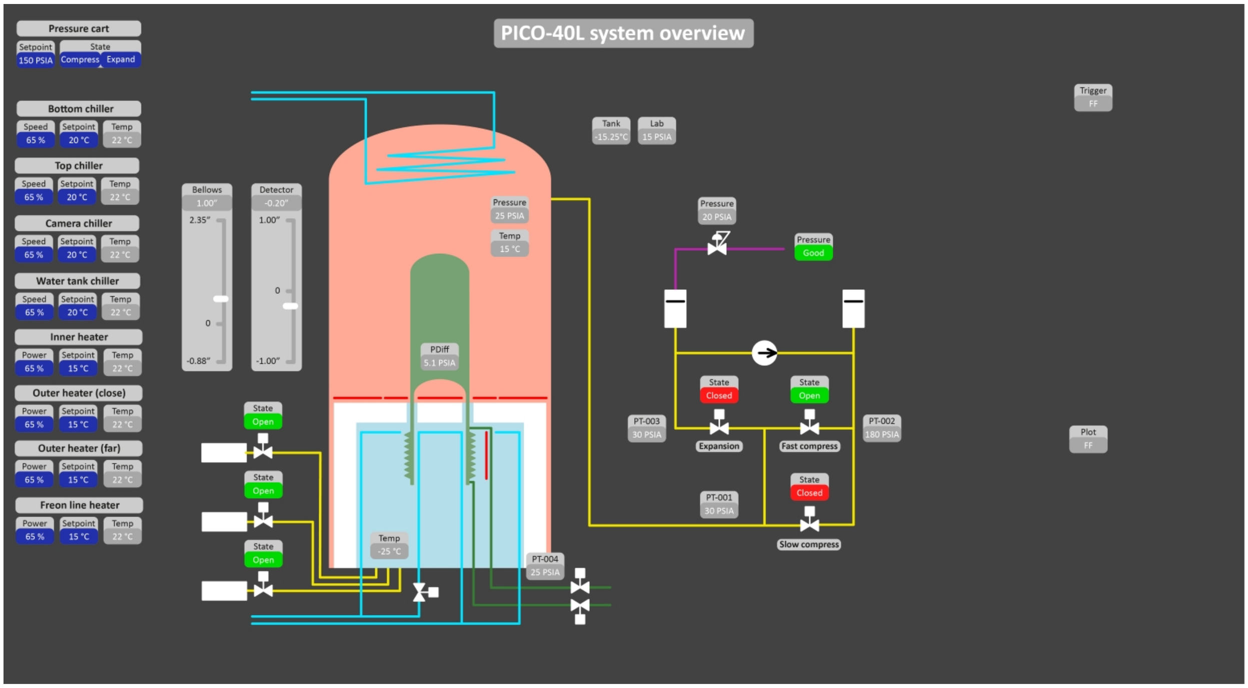

Pressure cart: Setpoint 150 PSIA; State Compress / Expand

Bottom chiller: Speed 65 %; Setpoint 20 °C; Temp 22 °C

Top chiller: Speed 65 %; Setpoint 20 °C; Temp 22 °C

Camera chiller: Speed 65 %; Setpoint 20 °C; Temp 22 °C

Water tank chiller: Speed 65 %; Setpoint 20 °C; Temp 22 °C

Inner heater: Power 65 %; Setpoint 15 °C; Temp 22 °C

Outer heater (close): Power 65 %; Setpoint 15 °C; Temp 22 °C

Outer heater (far): Power 65 %; Setpoint 15 °C; Temp 22 °C

Freon line heater: Power 65 %; Setpoint 15 °C; Temp 22 °C

Bellows 1.00″ (2.35″, 0, -0.88″)

Detector -0.20″ (1.00″, 0, -1.00″)

State Open
State Open
State Open

Temp -25 °C

PDiff 5.1 PSIA

Pressure 25 PSIA

Temp 15 °C

Tank -15.25°C

Lab 15 PSIA

Pressure 20 PSIA

Pressure Good

State Closed (Expansion)

State Open (Fast compress)

State Closed (Slow compress)

PT-003 30 PSIA

PT-002 180 PSIA

PT-001 30 PSIA

PT-004 25 PSIA

Trigger FF

Plot FF

Fig. 4.1. Layout of the overview tab displaying the important parameters of the detector.

4.1.1.1. *Labels and Buttons*

Various indicators for the slow DAQ are distinguishable by color. Figure 4.2 shows the common types of indicators and their meanings. There are other indicators such as the bars on the left of the detector that helps visualize the position of the bellows and the inner vessel.

Fig. 4.2. Example of the type of indicators in the slow DAQ. The red and green indicators reflect the state of a part of the detector and are denoted by either On/Off or Open/Closed. The blue indicators are buttons that are clickable and modified. Gray indicators are read-only static labels.

4.1.1.2. *Admin mode*

An admin mode was implemented in the program (top left corner of Figure 4.1) to prevent any accidental changes to the state of the detector. The admin prompt, accessible through any tab, requires a predetermined password (Figure 4.3 (left)) giving a 900-second access to the user to make changes to the detector and can be refreshed by reentering the password. Any user that does not have admin access will only be in a read-only mode and presented with the message shown in Figure 4.3 (right).

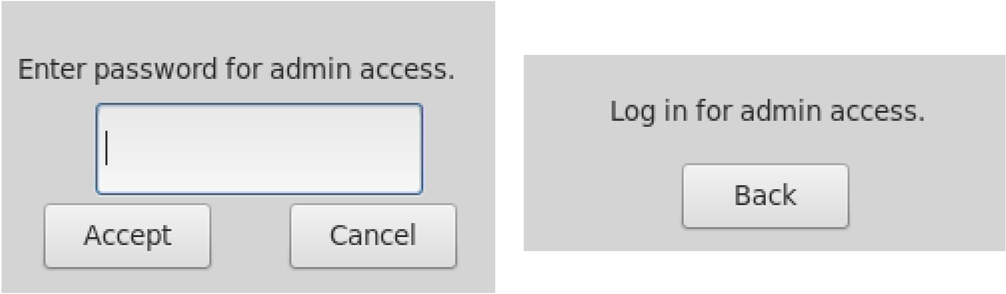
Enter password for admin access.

Log in for admin access.

Fig. 4.3. Left: Prompt for admin access to be able to make changes to the detector. **Right:** Error message denying any attempts to change the system without admin access.

4.1.1.3. *Plotting tool*

The overview tab will feature a plotting tool on the right side that will allow the user to select up to four parameters to plot as a function of time. An external plotting software is opened and provides real-time updating plots of the given parameters. Because the plotting software is independent of the main UI, it can also be accessed from the command line.

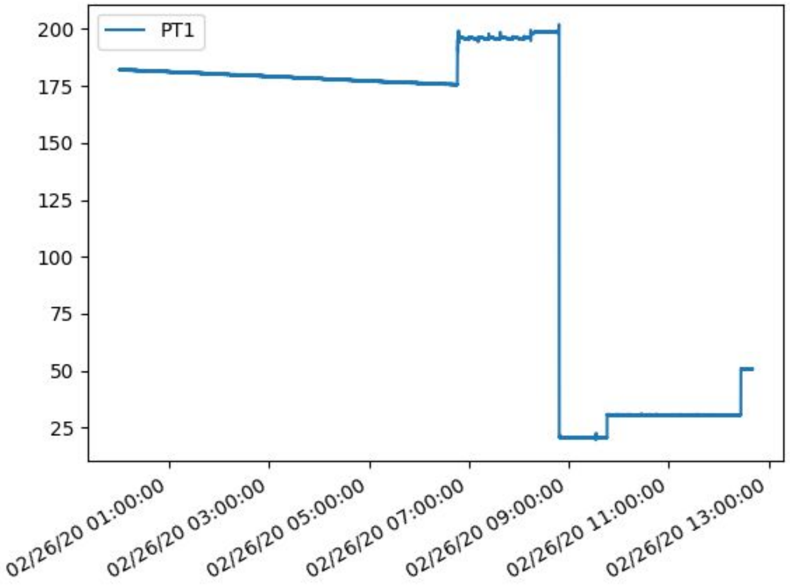

Fig. 4.4. Example of a plot from the slow DAQ. The plot shown displays the pressure of PT1 (Pressure Transducer measuring the pressure inside the outer jar) of PICO-40L as a function of time over the span of 12 hours. The variation in pressure in this plot shows the compressed state at high pressure and expanded state at low pressure during the testing phase.

4.1.2. Hydraulic System

The hydraulic system displays and controls the pressure system of the detector. This tab is utilized to visualize and change the state of different valves as a method of regulating the inner vessel's pressure. Figure 4.5 shows the design of the hydraulic system tab

4.1.3. Temperature System

The temperature system tab displays all the temperature-related sensors inside the detector. The majority of the sensors are resistance temperature detectors (RTDs) located in

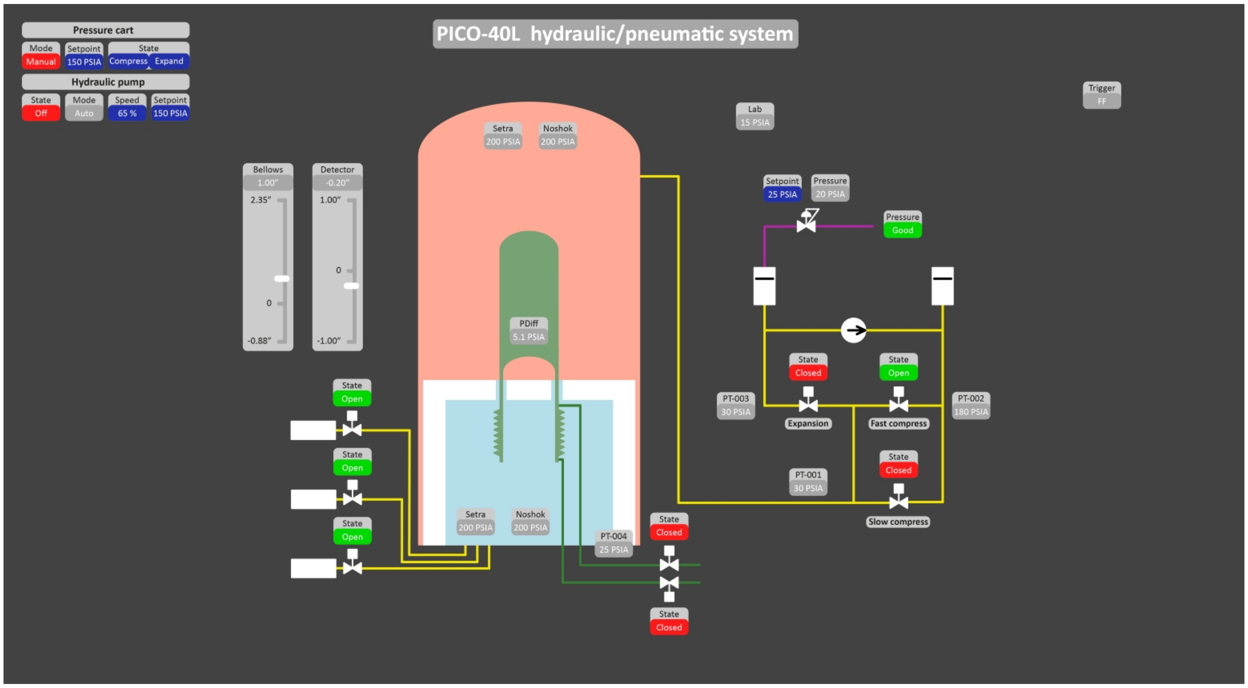
PICO-40L hydraulic/pneumatic system

Pressure cart
Mode: Manual
Setpoint: 150 PSIA
State: Compress Expand

Hydraulic pump
State: Off
Mode: Auto
Speed: 65 %
Setpoint: 150 PSIA

Trigger: FF
Lab: 15 PSIA
Setra: 200 PSIA
Noshok: 200 PSIA
Bellows: 1.00"
Detector: -0.20"
Setpoint: 25 PSIA
Pressure: 20 PSIA
Pressure: Good
PDiff: 5.1 PSIA
State: Closed
State: Open
PT-003: 30 PSIA
PT-002: 180 PSIA
State: Closed
PT-001: 30 PSIA
State: Open
State: Open
State: Open
Setra: 200 PSIA
Noshok: 200 PSIA
PT-004: 25 PSIA
State: Closed
State: Closed

Fig. 4.5. Layout of the hydraulic system tab for pressure readouts and valve control.

places where temperature readouts are crucial in order to properly monitor the operating conditions. On the left side of the UI, chillers and heaters can be turned on and off and the temperature setpoint can be adjusted as well. In addition, the PID parameters dictating the automatic temperature controls of the hot region (denoted by the light red color in the background), cold region (denoted by the sky blue color in the background) and the camera can be modified through this program. Finally, the conditions, such as temperature, humidity, and pressure, of all four cameras on the pressure vessel are monitored and the temperature of these cameras can be adjusted with the camera chiller button. Figure 4.6 show the design of the temperature tab.

4.1.4. Water System

The water system tab is the last tab on the UI and is used to control and monitor the conditions of the outer water tank. RTDs are placed inside the tank to monitor the temperature of the water. The water tank chiller parameters can also be adjusted to change the temperature of the water. Furthermore, certain valves can be opened and closed to dictate the flow between the water inside and outside the tank.

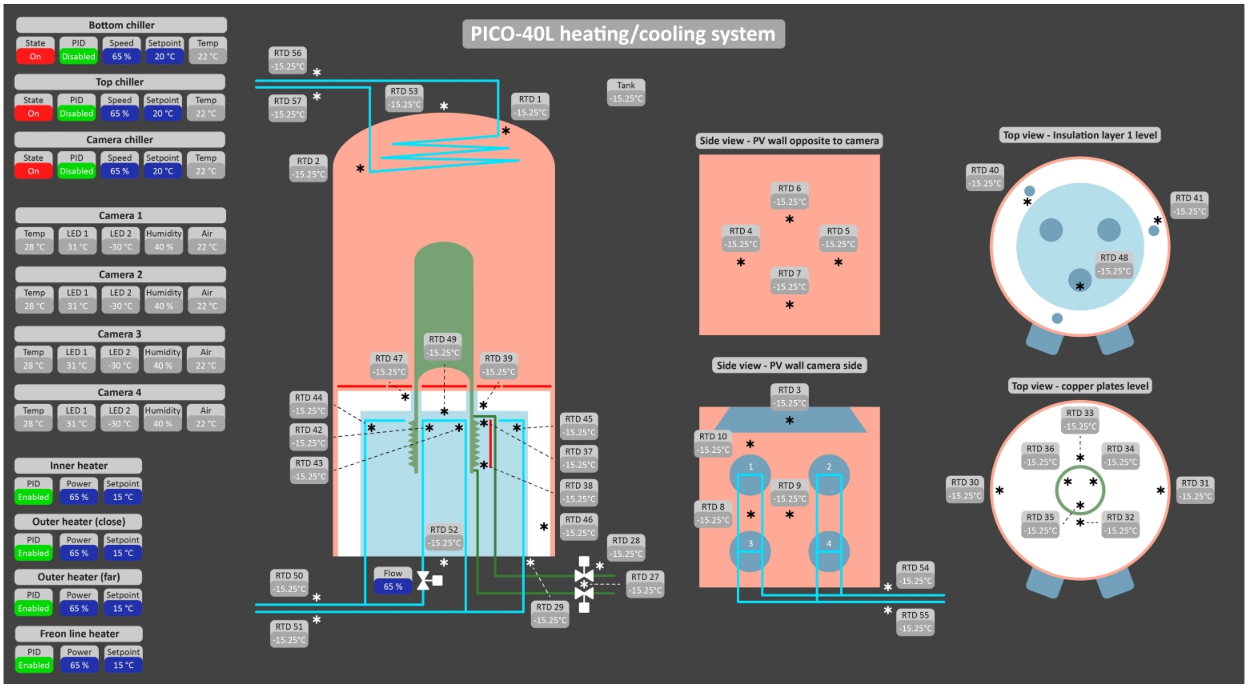

Bottom chiller

State	PID	Speed	Setpoint	Temp
On	Disabled	65 %	20 °C	22 °C

Top chiller

State	PID	Speed	Setpoint	Temp
On	Disabled	65 %	20 °C	22 °C

Camera chiller

State	PID	Speed	Setpoint	Temp
On	Disabled	65 %	20 °C	22 °C

Camera 1

Temp	LED 1	LED 2	Humidity	Air
28 °C	31 °C	-30 °C	40 %	22 °C

Camera 2

Temp	LED 1	LED 2	Humidity	Air
28 °C	31 °C	-30 °C	40 %	22 °C

Camera 3

Temp	LED 1	LED 2	Humidity	Air
28 °C	31 °C	-30 °C	40 %	22 °C

Camera 4

Temp	LED 1	LED 2	Humidity	Air
28 °C	31 °C	-30 °C	40 %	22 °C

Inner heater

PID	Power	Setpoint
Enabled	65 %	15 °C

Outer heater (close)

PID	Power	Setpoint
Enabled	65 %	15 °C

Outer heater (far)

PID	Power	Setpoint
Enabled	65 %	15 °C

Freon line heater

PID	Power	Setpoint
Enabled	65 %	15 °C

Fig. 4.6. Layout of the temperature system tab for temperature readouts, camera readouts, and chiller/heater controls.

4.2. Back end of the SlowDAQ Monitoring UI

The front end of the monitoring UI program is held together by multiple programming languages and codes. The diagram presented in Figure 4.7 summarizes the steps taken to provide a finished product. Further information is presented in the following subsections.

4.2.1. UI Design

The graphic element of the user interface is coded with Glade, an interface designer that allows the user to place different kinds of widgets on a designated window and compiles all the information regarding this window, such as widget positions and sizes, into an Extensible Markup File (XML) to be read by another code that manages the signals associated to the widget. Every indicator is shown in Figure 4.2 is associated with a dynamic text label to display a value. For blue indicators, a button widget is stacked on top of the label and associated with a click signal to create a clickable area.

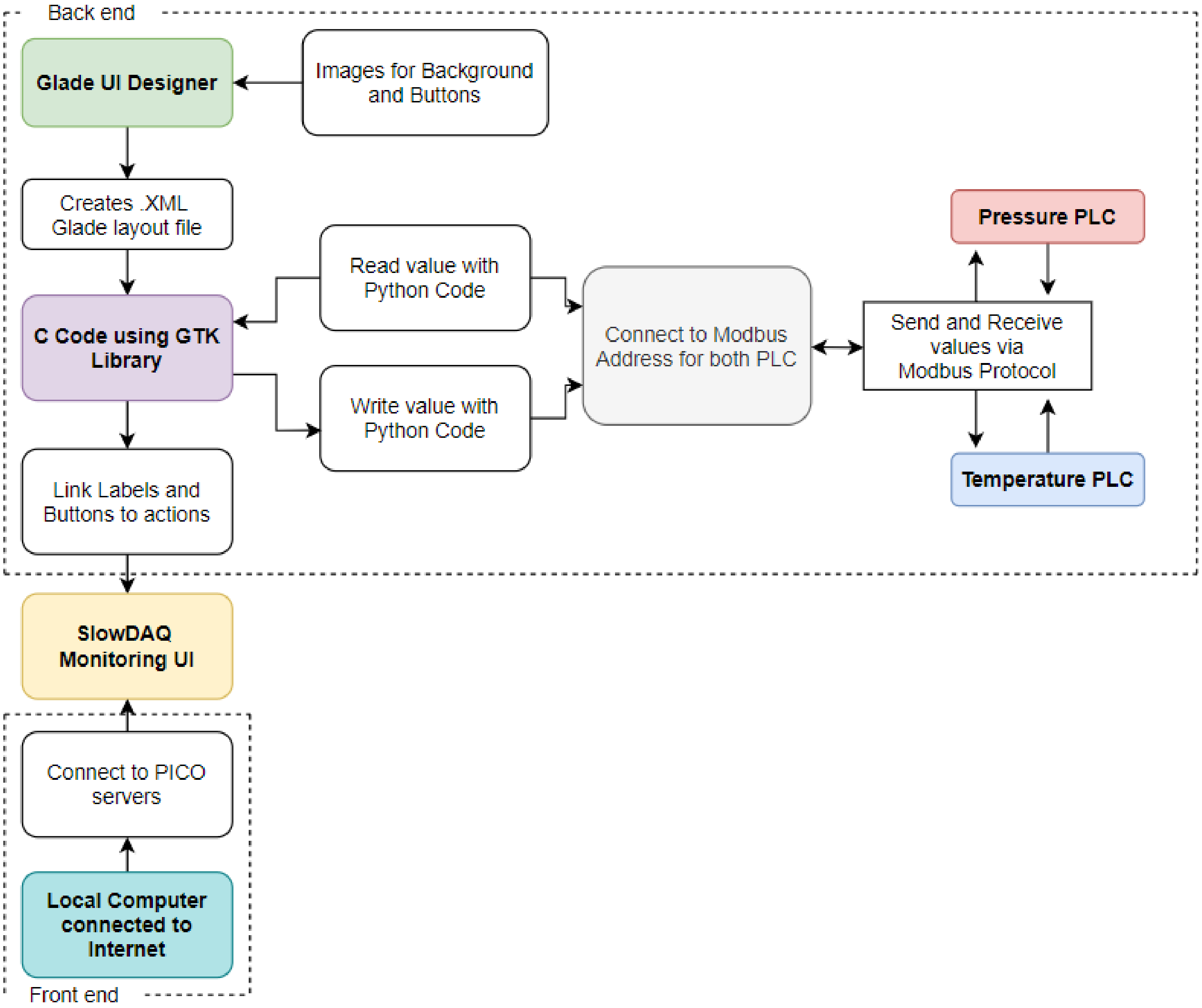

Fig. 4.7. Diagram showing how the UI reads and writes information to the detector through a series of codes. The layout is made with the Glade UI Designer (green), supported by a C code that utilizes the GTK library (purple) to read and write from both the pressure (red) and temperature (blue) PLCs. The output UI (yellow) is created and can be accessed from any computer (teal).

4.2.2. Code

The C based code supporting the interface is tasked to change the labels off read values, create a trigger signal for the buttons and send user inputs to the detector. The code starts by reading the UI information contained within the .XML file described in Section 4.2.1 as a structure for the code.

4.2.2.1. *Connecting to Modbus*

To read and write values from and to the detector, a Python code was written by the collaboration and then modified for the specific needs of this program. The Modbus protocol, a system that universalizes communication between different components of DAQ machines, is used for the exchange of values between the code and the on-site DAQ. Each readout such as pressure, temperature, and state from both the pressure PLC and the temperature PLC has an associated Modbus address to it and can be retrieved from this algorithm. Parameters of this code are exchanged between the C code and the Python code via a library designated for cross-language interpretation.

4.2.2.2. *GTK*

In the main C code, the GTK library is used to link all the widgets and declare them as variables inside the code to be able to manipulate them. Also, other functions in the library proved to be very useful such as the ability to dynamically change the labels based on a predetermined fixed interval of time and display the variables retrieved from the Python code.

4.3. Database Logging and Alarms

Another goal of the slow DAQ system was to create a running program that is able to log all the data and send out alarms based on the alarm conditions. This program is written by Chen Wen Chao and is independent of the monitoring UI described previously. The database logging script is written in Python based on the MySQL database managing system and compiled using Cython. The diagram presented in Figure 4.8 shows a flowchart of how the logging and alarm process works and will be further explained in the text.

The .XML files provided by the pressure PLC and temperature PLC contains the following information:

- PLC server address
- Modbus address for each variable
- Alarm conditions for each variable

The script begins by retrieving all the variables from both of the files and generating an alarm list based on the preset conditions. The script then accesses the PLCs via Modbus,

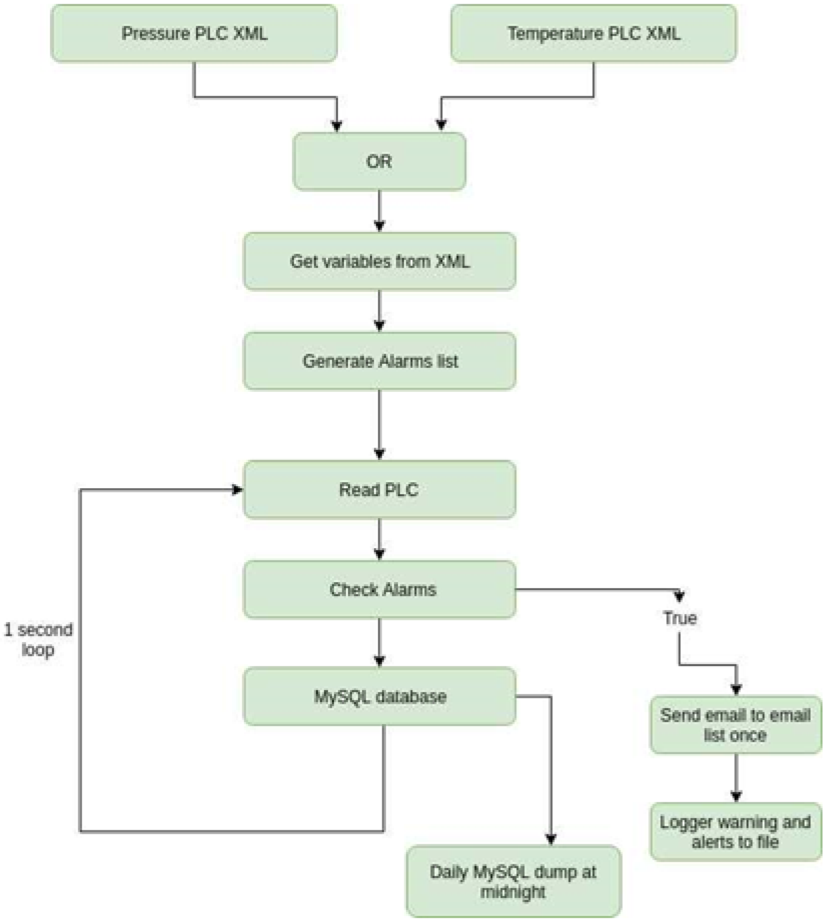

Fig. 4.8. Diagram of how the database logging system functions. Two .XML files from both pressure and temperature PLCs are read, alarm conditions are checked and recorded to the database.

reads all the variables, and checks whether any of the alarm conditions are met. Finally, the variables are then stored in a MySQL database and the script loops back to reading the PLC every second. Every day at midnight, the MySQL database is dumped and stored into the servers.

In the case where one of the alarm conditions is triggered, email and SMS alerts are sent to a designated list of recipients. If the condition of the alarm is unchanged within a set interval of time, a reminder is sent until it is corrected. A user can edit the state of the alarms and the email/SMS list through instructions given in the documentation.

Chapter 5

PICO-0.1 Detector

Multiple smaller test chambers are engineered for the purpose of calibrating the bigger bubble chambers such as PICO-40L. At Université de Montréal, the PICO-0.1 bubble chamber is used to calibrate the response of different types of particles, including gammas. This chapter will describe and present the detector itself while Chapter 6 will describe the coherent photon scattering measurement made using this detector.

5.1. Setup

The PICO-0.1 detector was built by Fermilab as a small version of a real PICO detector used for calibrations. It follows the same idea as a traditional PICO bubble chamber explained in Section 2.3.2. Figure 5.1 shows the setup of PICO-0.1 and lists its main components. The setup is further explained in the following sections with number references to the figure.

The fused silica pressure vessel (1), a XQ80 designed for high-pressure chemical reactions, can hold up to 75 ml of target fluid and is held on by a stand. The jar is able to withstand high pressures provided by the hydraulic system (4) without the need for a pressure vessel due to its thicker walls of 0.9 cm and small radius. The pressure system is comprised of two accumulators, one for high pressure (over 150 PSIA) and one for low pressure (20-70 PSIA), filled with mineral oil, and is regulated by electronic valves controlled by a National Instruments synchronous controller and asynchronous DAQ computer using Labview linked to it. The top hat shaped bellow system (3) is filled with oil and two steel bellows. Figure 5.2 shows the inside of the top hat when it is removed. The pressure inside the jar is controlled by changing the compressing and expanding the bellows with the hydraulic system. The

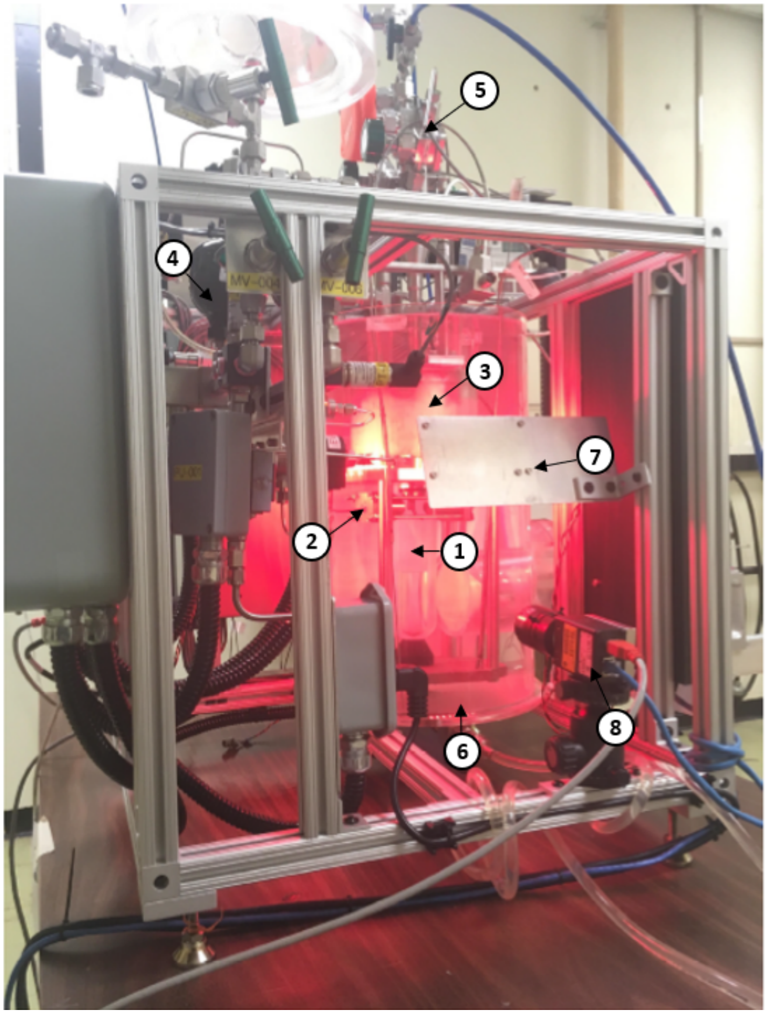

Fig. 5.1. PICO-0.1 setup: **1**. Fused silica jar, **2**. Piezoelectric sensors, **3**. Top hat containing bellows, **4**. Pressure system, **5**. Valve system for feeding and evacuating fluids, **6**. Water bath, **7**. LEDs, **8**. One of two camera.

valve system on top of the bellows (5) is used to fill the jar with oil, which is used as a buffer, and target fluid. After the initial fill, an oil-filled capsule and a bleeding port are used to maintain a low-pressure differential between the outside and inside of the bellows by either adding or removing the buffer oil, this is mainly to prevent putting too much pressure on the bellows and breaking them. Two piezoelectric sensors (2) are installed near the top of the jar to capture the acoustic signals produced by the bubbles. However, due to the thickness of the jar, the signal read by the piezos is limited in amplitude and are not used for the measurement described in Chapter 6. The detector is placed inside a water-filled bath (6) connected to an external chiller to control the temperature within the detector. Four temperature sensors are placed inside the bath at different heights to monitor the temperature gradient within the bath. Four pressure transducers placed at key spots are used to monitor the pressure of the accumulators, the pressure regulator, the bellows, and the target fluid. The pressure and temperature sensors are required to be able to calibrate the threshold of the detector to prevent any damage to the detector caused by overpressure. Two sets of LEDs (6) are used to add brightness to the picture quality produced by both cameras (8).

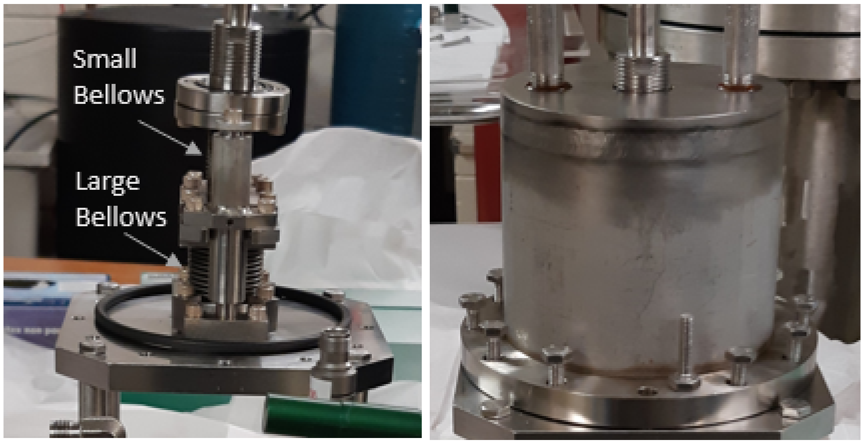

Fig. 5.2. Left: Bellows system inside of the cover regulating the pressure inside the jar during operations. **Right**: Close up of the top hat of the detector containing the bellows system.

5.2. Assembly and Tests

Before taking any calibration measurements using the PICO-0.1 bubble chamber, the detector is to be disassembled, cleaned, reassembled, filled, and tested to ensure the quality of the data during the measurement. After previous measurements, the detector is usually left in an idle compressed state and ready to either take new measurements or to be reassembled with a new target fluid. Even when using the same fluid, a reassembly is also recommended if the previous calibration was lengthy. This is mainly due to the possibility of passive condensation of gaseous freon inside the bellows section of the detector leading to spontaneous boiling that limits the operable setpoint expansion pressure. Because of the smaller size of this detector compared to PICO-60 or PICO-40L, the active fluid can be easily and quickly changed for different calibration measurements.

After disassembly, the components of the detector are thoroughly cleaned to prevent any unwanted bubble events during the run phase due to residual particles. Because most of the components have been in contact with some sort of oil in the previous assembly, multiple rounds of cleaning are performed in order to ensure that no oil is left on any piece before the final assembly. All the non-electronic components are hand cleaned with soap and water to remove the majority of the oil. Afterward, inside an ISO 4 cleanroom, the components are then placed inside an ultrasonic bath to be washed once with RadiacWash for around 30-45 minutes and once without for 20-30 minutes. Finally, the final reassembly of the detector is done in an ISO 3 cleanroom to minimize unwanted particles coming in contact with the inside of the jar. Some external components, such as the stand, do not need to be meticulously cleaned since they will be in contact with oil anyways during the assembly

A leak check is done using a helium leak detector to verify that all seals are properly done and that there no possibility of a leak after the assembly. After adding oil as the buffer, a procedure describes the steps to follow to fill the outside of the bellows with mineral oil and to pressurize the accumulators. The active fluid is slowly fed through the valve system through condensation until an appropriate amount of liquid has been added to the jar. Careful attention must be given during the fill since the droplets can start to condensate inside the bellows if the flow is too fast. Any liquid stuck inside the steel bellows can cause instabilities during the data acquisition and cannot be easily removed without doing a full disassembly.

5.3. Stability Tests

With the fill complete, the testing phase begins by constantly expanding and compressing the detector using the DAQ computer to verify that the pressure drop and rise are consistent. In a previous testing phase, the pressure dropped noticeably slower than expected and was unable to reach the designated set point. In addition, the pressure inside the jar and the oil inside the top hat was slowly equalizing, meaning that there was a possibility of a leak causing fluid to be exchanged between both systems and is further explained in the following section. If the detector shows no sign of problems when compressing and expanding, the next step is to test the threshold range of the detector to see whether or not it can reliably reach the pressure it has to for the desired calibration measurements.

5.4. 2018 Assembly and Tests

To perform the measurements explained in Chapter 6, the assembly of the detector and fill with C_3F_8 as the active fluid, following the $C_2H_2F_4$ calibrations by Frédéric Tardif, was done in late 2018. During the assembly, it was noticed that the small bellows were not straight, but a bit crooked. This was most likely caused by unintentionally large forces applied to them due to undetected leaks or poor handling. After performing a helium leak test on both bellows, it was concluded that no apparent leaks were present. Although the assembly went smoothly, a major issue was seen during expansion and compression tests while testing for stability shown in Figure 5.3.

After several expansion and compression cycles, the detector was not able to reach the pressure set point and the pressure inside the regulating bellows was slowly going down. In addition, the pressure differential between the pressure inside bellows and the pressure in the jar was slowly going towards 0 in both the expanded and compressed state, it was clear that the integrity of the detector had been compromised. It was suspected that the slightly crooked small bellows ended up breaking and was leaking causing an exchange of fluids between the outside of the bellows and the inside, eventually equalizing the pressures. After the disassembly, it was clear that the small bellows were already on its last legs. Figure 5.4 shows a picture of the deformed bellows right after the removal of the top hat.

A thorough inspection of the bellows confirmed that some areas of the bellow convolutions were ripped. The first idea was to replace the existing bellows with a spare part within the collaboration, but to no avail since no spare bellows with similar specifications were available. The second idea was to solder the teared parts of the bellow to be able to reseal them, but even after the soldering, a helium leak test still indicated a large leak. The final solution was to find a manufacturer that sells stainless steel bellows with similar specifications. Most of the companies that were contacted replied that to produce these stainless steel bellows, they would need to make custom molds, which made the cost over the expected budget. Fortunately, a company was able to sell similar bellows that were already in stock at a moderate cost. However, miscommunications and disagreement over payment terms caused the shipment to arrive much later than expected, which delayed the progress of the project. Upon the arrival of the bellows, the previous flanges were soldered onto them and a leak test was performed to ensure everything was working as intended.

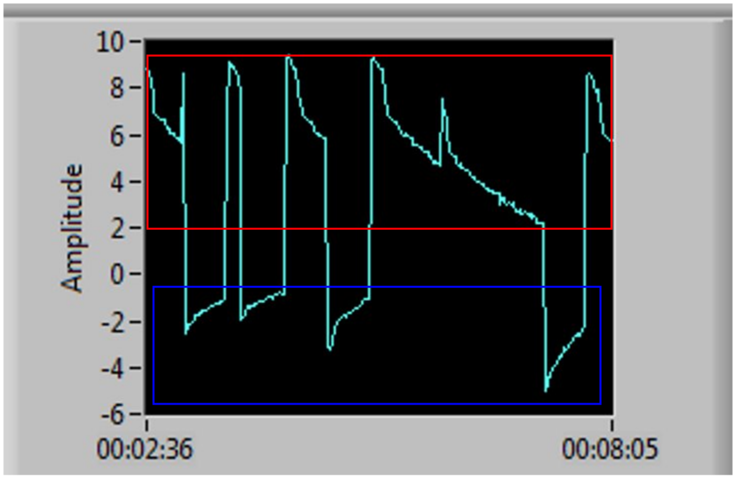

Fig. 5.3. Plot of the pressure differential between the pressure inside the jar (active fluid) and the regulating pressure at the bellows for multiple cycles. The expanded states is shown in red and the compressed states are shown in blue. The pressure differential goes towards 0 in both the expanded and compressed state.

5.5. The Future of PICO-0.1

PICO-0.1 will remain an important tool used to make important measurements at Université de Montréal. Following the coherent photon scattering measurement presented in Chapter 6, an attempt to measure the directionality of bubble events inside PICO-0.1 will be made by applying an electric field to the active fluid inside the quartz jar. Further down the line, there will be plans to change the detector to the "right-side up" design like PICO-40L, which will allow further testing of this new technology.

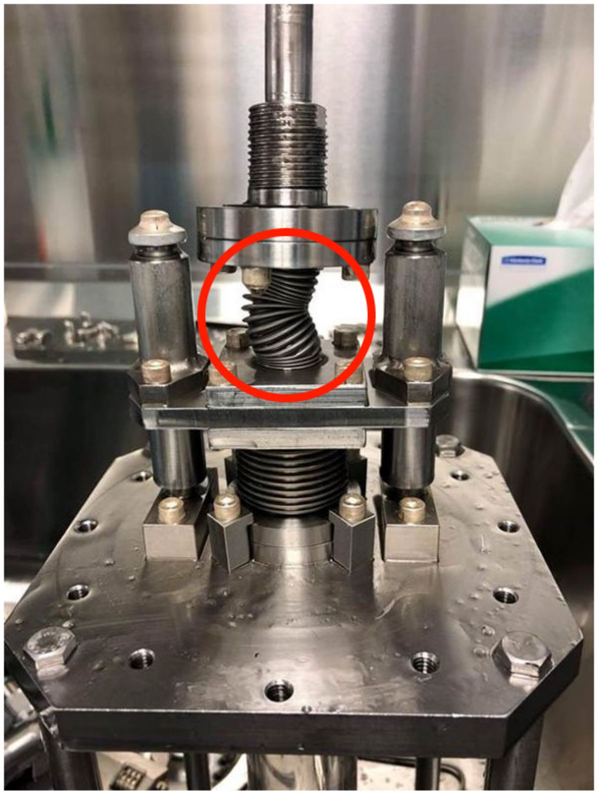

Fig. 5.4. Picture of the bellows of PICO-0.1 after the removal of the top hat following tests showing instabilities inside the detector. This kind of deformity (shown in red) can trap condensed freon inside the bellows, hindering the normal operation of the detector.

Chapter 6

Coherent Photon Scattering Measurements

With direct dark matter experiments being unable to claim a dark matter signal in the current energy scale in both the spin-independent (Figure 1.3) and spin-dependent (Figure 1.4), future detectors of these experiments will have to explore lower energy scales. As a consequence, recoils produced by lower energy particles such as CEvNS (Section 1.6) will start dominating background events. Amongst these backgrounds, MeV-scale photons scattering off the atom of the target can create a recoil signal within the detector at sub-keV thresholds. This coherent (nuclear Thomson) photon scattering will start to become a significant background for experiments running at low thresholds like SuperCDMS, which leads to future detectors having to decide to either invest resources into mitigating it or develop a discriminating technique to isolate this type of produced signal [**41**].

Although it is unlikely that future PICO bubble chambers will be able to achieve this sub-keV threshold, the PICO-0.1 chamber filled with C_3F_8 as the active fluid described in Chapter 5 can be used in the prescence of a source to provide the world's first measurement of this effect. To produce recoils above the PICO detection threshold of several keV, high energy photons of 6.13, 6.92, and 7.12 MeV are produced using Université de Montréal's Tandem accelerator. These high energy gammas are produced through the $^{19}F(p,\alpha\gamma)^{16}O$ interaction by creating a proton beam hitting a CaF_2 target. The C_3F_8 filled PICO-0.1 detector is placed in proximity of the target producing gammas to record the events. Previously, Frédéric Tardif had attempted to measure this Thomson scattering with the $C_2H_2F_4$ filled PICO-0.1 bubble chamber but was unsuccessful due to the high background events caused by low-energy neutrons from the dissociation of deuterium inside the active fluid itself [**47**].

To detect nuclear Thomson scattering, this measurement looks for a significant increase in the number of bubble events inside the detector at specific threshold energies. It is also necessary to evaluate and measure all possible backgrounds that can affect the results.

6.1. Université de Montréal Particle Accelerator

One of the advantages of operating PICO-0.1 at Université de Montréal is the different types of interactions that can be produced using the particle accelerator. This tandem based accelerator utilizes a two-step ion acceleration process through a high voltage terminal to produce the desired particles. The beam current is prepared and optimized in the control room by manipulating different deflectors to finally hit the desired target. The floor plan of the particle accelerator is shown in Figure 6.1.

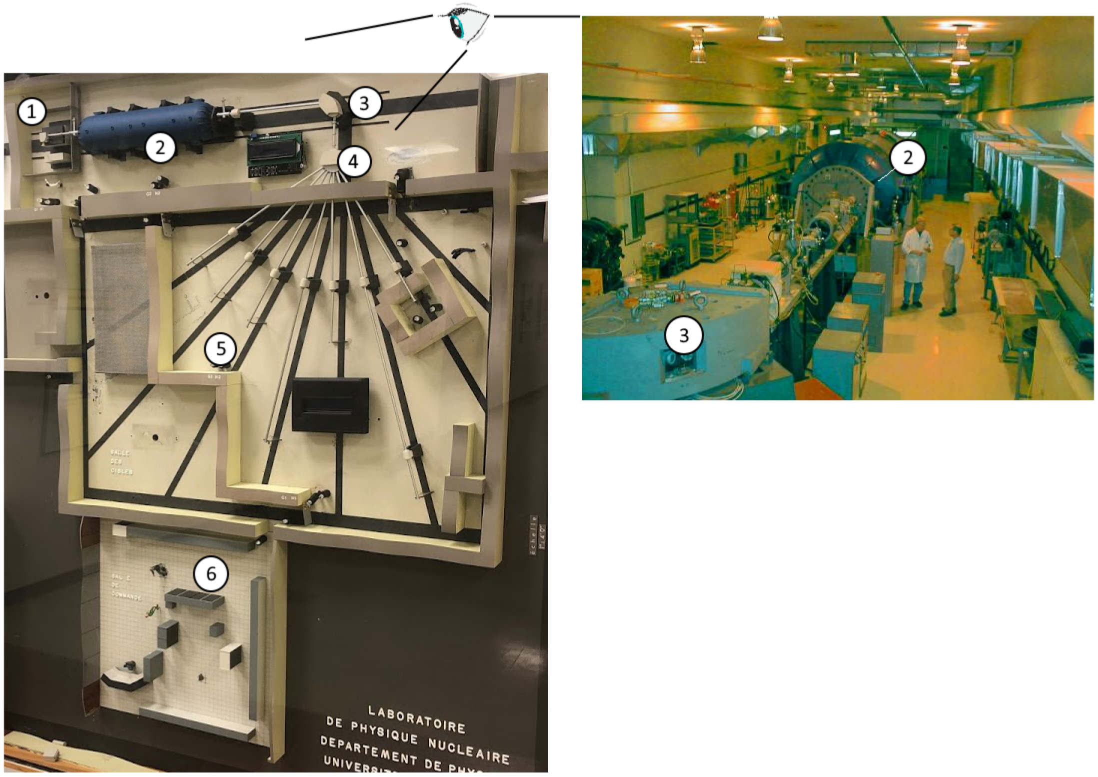

Fig. 6.1. Plan of Université de Montréal's particle accelerator. **1**: Source. **2**: Tandem accelerator. **3**: Analysing magnet. **4**: Faraday cage and switching magnet. **5**: Target room. **6**: Control room.

A source is placed at the beginning of the line (1) to be stripped and accelerated by the tandem (2). The beam passes through a magnetic deflector (3) before the Faraday cage (4) and split to the desired beamline in the target room (5) where the detector lies. The control room (6) electronically operates the beam in a radiation safe area. A safety procedure is followed and multiple radiation counters are placed around the room to ensure the security of anybody working in the facility.

6.2. Mechanism

There are a few sub-GeV interactions that can occur with a photon: incoherent scattering (Compton or Thomson), coherent scattering (Rayleigh, Delbrück, nuclear Thomson or nuclear resonance), photoabsorption, pair production, and photonuclear reactions. The interaction of interest here is the nuclear Thomson scattering, which occurs when energy from photon is deposited onto a nucleus and creates a recoil. For eV scale direct dark matter experiments, coherent scattering dominates over incoherent (Compton) scattering and will produce an enhanced spectrum of low-energy recoils [**41**]. For this measurement, at the energy scale of the gamma source, the detector is highly sensitive to this interaction. Figure 6.2 depicts a simplified example of a single interaction that can occur within the detector.

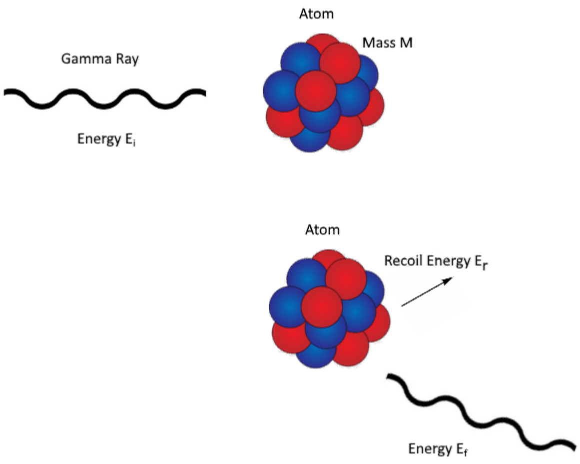

Fig. 6.2. An incoming gamma ray with energy E_i hits the atom of the target fluid, is backscattered with energy E_f, and produces a recoil energy that is recorded if the recoil energy E_r meets the threshold requirement of the operating conditions.

The recoil energy produced by this interaction is given by:

$$E_r = \frac{(2E_\gamma \sin\frac{1}{2}\theta)^2}{2Mc^2} \tag{6.2.1}$$

where E_γ is the gamma energy, θ is the angle of interaction, and M is the mass of the atom. The maximum recoil energies for gamma rays backscattering from either the ^{12}C and ^{19}F atoms are listed in Table 6.1.

Gamma Energy (MeV)	Carbon Recoil (keV)	Fluorine Recoil (keV)
6.13	6.66	4.20
6.92	8.52	5.38
7.12	9.02	5.70

Tab. 6.1. Recoil energy of the interaction between the gamma ray at a specific energy and both the ^{12}C and ^{19}F atoms.

6.3. Experimental Setup

The PICO-0.1 detector setup is placed at the end of Université de Montréal's 0 degree beamline (line perpendicular to the Tandem accelerator in Figure 6.1) to be exposed to the produced gamma rays. While the beam is running, the DAQ is remotely accessed through a computer connected to the virtual network in the particle accelerator's control room to be able to safely control the detector settings. The experimental setup of this calibration is depicted in Figure 6.3.

The BGO detector is used in order to measure the relative bubble nucleation probability of PICO-0.1. A discriminator with a narrow acceptance window, set around the 6.13 MeV peak, provided a measure of the photon fluence in that region. The signal is stretched and then digitized by the DAQ. The slow digitization rate of the DAQ necessitated a relatively low count rate to prevent pileup. As a result, an extremely narrow discriminator window was chosen and the BGO was placed further away from the photon production source.

6.4. Expected Backgrounds

As for most measurements, there are expected backgrounds that will have to be taken into account during the analysis of the results.

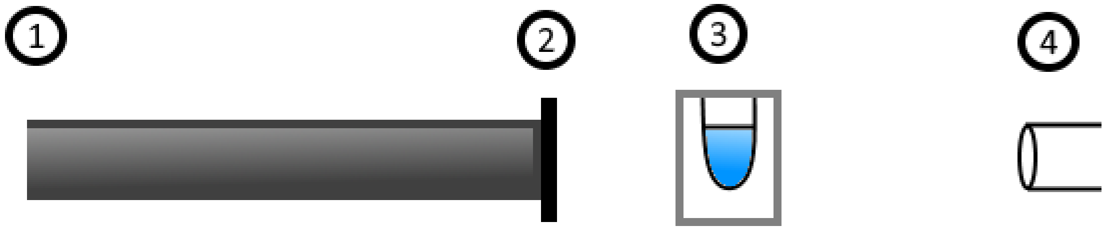

Fig. 6.3. Experimental setup of the calibration. Protons produced by the particle accelerator (1) interacts with the CaF_2 target (2) placed at the end to create gammas. The PICO-0.1 detector (3) is placed 24.5 cm away from the target to be exposed to the produced gamma rays. A 7.6 cm diameter and 5 cm thick Bismuth Germanate (BGO) based gamma counter pointed towards the PICO-0.1 detector (4) is placed 157 cm away from the target to measure the relative number of events occurring in PICO-0.1 during the analysis.

6.4.1. Environmental Background

These are background events from ambient interactions. This can include neutrons and gammas from the environment interacting with the active fluid during the run. To correct for this background, events are recorded by PICO-0.1 for several days without the gamma source and are subtracted from the real run dataset. Events caused by this background are expected to be minimal since gammas that will interact with the active fluid are not abundant in the environment and the bath of water surrounding the jar is also used as shielding against neutrons.

Also, alpha events produced by the decay chain of ^{222}Rn are expected to have nuclear recoils of over 100 keV and are nearly 100% efficient [**26, 20**]. Although this presents itself as a significant background to the experiment, its contribution can be estimated by recording higher threshold events outside of the region of interest but lower than 100 keV to keep its high bubble nucleation efficiency.

6.4.2. Deuterium Background

The limiting factor of Frédéric Tardif's attempt at measuring this coherent photon scattering was the presence of dissociating deuterium in the $C_2H_2F_4$. Although the C_3F_8 does not contain hydrogen, the water bath surrounding the active fluid may be a background.

To see whether or not this background is significant, 1g of fully deuterated styrene sample, which contains as much deuterium as about 64L of ordinary water, was placed between the beam and the detector, and the event rate was examined. A significantly enhanced rate of events from deuterium dissociation would be expected in the presence of this additional deuterium, providing an upper limit on the rate of this process in the 1 L of water surrounding the detector from which low energy neutrons could efficiently enter the detector and produce a bubble

6.4.3. Other Beam-on Backgrounds

Alpha events produced by the decay chain of ^{222}Rn are expected to have nuclear recoils of over 100 keV and are nearly 100% efficient [**26, 20**]. Although this presents itself as a significant background to the experiment, its contribution can be estimated by recording higher threshold events outside of the region of interest but lower than 100 keV to keep its high bubble nucleation efficiency.

6.5. Production of Gamma Ray

To produce the gamma rays of the specified energy for the experiment, the accelerator process explained in Section 6.1 is used. The source and beam were set up to produce a 1.4 MeV proton beam to collide with the CaF_2 target of several nm thick at the end of the beamline. This documented production method explained in [**49**] is able to produce 6.13, 6.92, and 7.12 MeV gamma rays used for this calibration through the ^{19}F(p,$\alpha\gamma$)^{16}O reaction. The mechanism of this reaction exploits the high energy gamma emission from energy level transitions of the excited states of ^{16}O.

After setting up Université de Montréal's particle accelerator to produce the desired proton beam energy and optimal beamwidth with the help of an operator, a test run was done to measure the frequency of bubble events inside the jar. For a good data set, the time it takes for a bubble to be produced has to be long enough so that the possibility of two overlapping events is as low as possible but it has to be fast enough so that as much data as possible can be recorded during the data acquisition period. After a couple of dozens of test events, the beam current was adjusted to be $(0.80 \pm 0.02)\mu$A such that events were occurring on average at about 10 to 15 seconds after the beam starts at the lowest threshold operating conditions. The uncertainty on the current is estimated by observing of the current monitor in the control room.

6.6. Run Conditions

Before the data acquisition period, the PICO-0.1 detector settings have to be set at the desired temperature and pressure conditions. Options in the DAQ gives the user the choice to provide multiple settings of pressure during the run. Then the program randomly selects the pressure of the next expansion after each event based on the given weight of each input. The randomization of the pressure setpoints is to avoid any bias due to time varying backgrounds within the run. The C_3F_8 filled chamber calibration run had two independent data acquisition periods and the approximate run conditions are shown in Table 6.6 for the first run and Table 6.7 for the second run. During both data acquisition periods, the temperature of the chiller was set at 14°C.

During the run, the DAQ sends an electrical signal to the software controlling the particle accelerator before the expansion to turn on the beam 10 seconds after the beginning of the expansion, this lets the detector reach the pressure set point before being exposed to the gammas. Once 10 seconds have elapsed, the beam starts, and gammas are produced via the ^{19}F(p,$\alpha\gamma$)^{16}O reaction.

6.7. Expected Number of Events

The expected number of events coming from the coherent photon scattering can be computed given the conditions of the setup. The first step is to figure out the number of gammas, which are produced via the ^{19}F(p,$\alpha\gamma$)^{16}O reaction using the 1.37 MeV resonance, reaching the active fluid inside PICO-0.1 after the production at the beamline and then account for the interaction cross section.

6.7.1. Photon production

The rate at which the photons are produced at the beam can be computed using the following equation:

$$\text{Yield} = \frac{\text{Avogadro Number} \times \text{Cross Section} \times \text{Resonance Width}}{\text{Stopping Power} \times \text{CaF}_2 \text{ Molar Mass}} \tag{6.7.1}$$

Where the stopping power of CaF_2 for 1.37 MeV protons was given by [**23**] and the interaction cross section and resonance width of the $^{19}F(p,\alpha\gamma)^{16}O$ reaction was provided by [**46**]. Table 6.2 summarizes the parameters used in equation 6.7.1.

Stopping Power (MeV cm^2 /g)	$(1.41\pm0.03)\times10^2$
CaF_2 Molar Mass (g/mol)	78.07
Avogadro's Number (/mol)	6.02×10^{23}
Interaction Cross Section (cm^2)	$(3.51\pm0.27)\times10^{-25}$
Cross Section Energy Width (MeV)	$(1.19\pm0.12)\times10^{-2}$
Proton Current (e/s)	$(5.0 \pm 0.1) \times 10^{12}$

Tab. 6.2. Summary of the variables used for the number of photons produced.

Using Equation 6.7.1, this leads to a photon production rate of $(2.3\pm0.3)\times10^6$ photons/s. The $^{19}F(p,\alpha\gamma)^{16}O$ reaction using 1.37 MeV protons produces 6.13, 6.92 and 7.12 MeV photons with a 92% yield and a branching ratio of 76.20%, 11.50%, and 4.30% respectively [**43**].

6.7.2. Mass attenuation

The second factor to take into account is the proportion of photons lost due to the mass attenuation of the material the photons will have to go through before reaching the active fluid. Given the highly penetrating photons, the scattering is negligible and a 1-dimensional model can be used to approximate this attenuation. Figure 6.4 depicts an example of the path of a photon.

To calculate the attenuation, Beer-Lambert's law describing the attenuation of light in the material its travelling inside is:

$$\text{Intensity} = e^{-\frac{\mu\lambda}{\rho_m}} \tag{6.7.2}$$

Where μ is the mass attenuation coefficient, λ is the area density, and ρ_m is the mass density. Table 6.3 lists the length of the medium and the density and Table 6.4 lists the attenuation coefficients provided by graphs taken from the National Institute of Standards and Technology [**31**] and extracted by Engauge [**36**] and the final attenuation.

The total mass attenuation for 6.13, 6.92, and 7.12 MeV photons are $(89.2 \pm 2.0)\%$, $(89.6 \pm 2.0)\%$, and $(89.8 \pm 2.0)\%$ respectively.

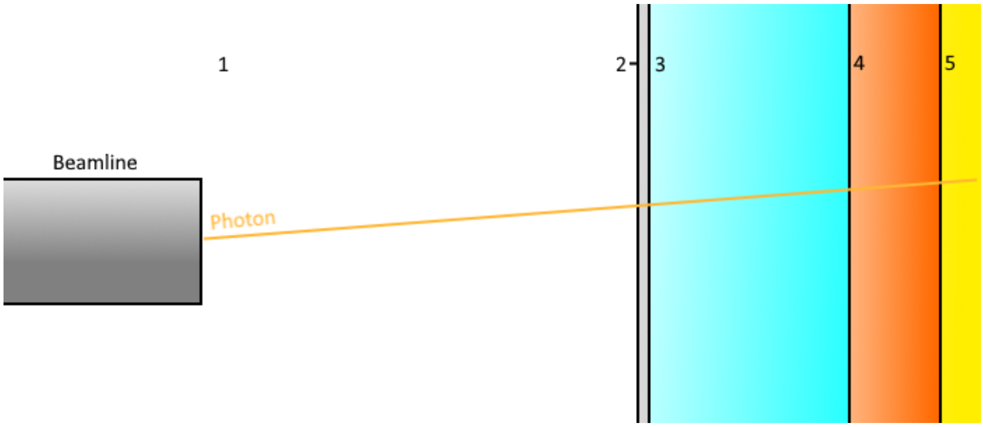

Fig. 6.4. The path of a photon coming out of the end of the beamline reaching the active fluid. It starts by goes through the air (1), then reaches the acrylic water bath wall (2), passes by the water (3), then the quartz jar (4) and finally reaches the active fluid (5). Half of the active fluid's volume is taken into consideration in this calculation.

Medium	Length (in cm)	Density (in g/cm^3)
Air (gas)	11.37	0.0012
Acrylic (solid)	0.63	1.18
Water (liquid)	10.35	0.00100
Quartz (solid)	0.902	2.2
C3F8 (liquid)	1.25	1.38

Tab. 6.3. Table of length in medium with their respective densities.

6.7.3. C_3F_8 Cross Section

The cross section for the nuclear Thomson scattering is given by:

$$\sigma_T = \frac{8\pi}{3}(\frac{\alpha\hbar Z^2}{mc})^2 \tag{6.7.3}$$

Where α is the fine structure constant, $\hbar$ is the reduced Planck constant, Z is the atomic number, m is the mass of the nucleus and c is the speed of light. Using this formula, the interaction cross section for on the nucleus is 8.89×10^{-8} cm^2/g for ^{12}C and 1.26×10^{-7} cm^2/g for ^{19}F. This gives a total cross section for C_3F_8 of 1.85×10^{-8} cm^2/g. From the density given in Table 6.3 and a volume of (25.0 ± 0.5) mL, the jar contained a total of (34.5 ± 0.7) g of C_3F_8. By multiplying the cross section by the photon production and taking into

Medium (Photon Energy)	Mass Attenuation Coefficient (in cm^2/g)	Intensity (in %)
Air (6.13 MeV)	0.0250	99.97±0.40
Air (6.92 MeV)	0.0238	99.97±0.42
Air (7.12 MeV)	0.0234	99.97±0.43
Acrylic (6.13 MeV)	0.0263	98.06±0.37
Acrylic (6.92 MeV)	0.0250	98.16±0.39
Acrylic (7.12 MeV)	0.0244	98.20±0.40
Water (6.13 MeV)	0.0277	99.97±0.36
Water (6.92 MeV)	0.0263	99.97±0.38
Water (7.12 MeV)	0.0258	99.97±0.39
SiO_2 (6.13 MeV)	0.0266	94.86±0.36
SiO_2 (6.92 MeV)	0.0255	95.07±0.37
SiO_2 (7.12 MeV)	0.0258	95.00±0.37
C_3F_8 (6.13 MeV)	0.0243	95.91±0.40
C_3F_8 (6.92 MeV)	0.0232	96.08±0.41
C_3F_8 (7.12 MeV)	0.0218	96.32±0.44

Tab. 6.4. X-Ray mass Coefficients in cm^2/g of each material a photon goes through for each photon energy provided by NIST. The error on each value is 0.0001 and reflects the uncertainty on the value that was extracted from Engauge. The intensity is computed using Equation 6.7.1.

account the mass attenuation, the mass of C_3F_8 and the mean distance between the source and the target fluid, the interaction rate is expected to be $(1.60 \pm 0.21)\times10^{-4}$ events/s.

6.7.4. Thomson Scattering Spectrum

To incorporate the expected PICO-0.1 response based on the operating conditions of the detector, the normalized integrated Thomson scattering spectrum formula calculated by Frédéric Tardif [**47**] is used:

$$R(E_{th}) = 1 - \frac{3}{4}\frac{mc^2}{E_\gamma^2}E_{th} + \frac{3}{8}(\frac{mc^2}{E_\gamma^2}E_{th})^2 - \frac{1}{8}(\frac{mc^2}{E_\gamma^2}E_{th})^3 \qquad (6.7.4)$$

Threshold (keV)	6.13 MeV	6.92 MeV	7.12 MeV	Total
2.6	0.458	0.550	0.569	0.475
3.2	0.350	0.473	0.496	0.372
3.9	0.194	0.376	0.407	0.228
5.0	0.081	0.188	0.242	0.102
6.4	0.016	0.080	0.090	0.028
8.7	0	0	0.013	0.001
12.1	0	0	0	0
17.8	0	0	0	0

Tab. 6.5. Table of the expected response of C_3F_8 filled PICO-0.1 bubble chamber at different energy thresholds for all 3 photon energies. The total expected response in the last column was calculated by taking into account the relative branching ratios given in Section 6.7.1.

Where m is the mass of the nucleus, E_{th} is the threshold energy, and E_γ is the energy of the gamma. Table 6.5 lists the expected response for C_3F_8 at all 3 photon energies.

6.8. Data Acquisition Period

The two data acquisition periods were in August 2019 and November 2019. During the first run, the BGO counter did not properly record gammas during the background run, possibly because it was looking at the wrong energy window. During the second run, a synchronization issue between the beam start signal and the actual start of the beam was present. After the expected 10-second expansion delay, the beam on signal in the DAQ was set to true while the beam took an extra couple of seconds to actually turn on. This permitted the detector to collect 'beam on' data without actual beam. The fix for this was to provide a return signal from one of the Faraday cages (4 of Figure 6.1) where the beam on boolean inside the DAQ would only turn true if a beam was detected. Events prior to the fix were kept and the live times were adjusted in the processing based on the first recorded gamma by the BGO detector.

6.9. Data Processing

After taking data, the data itself is stored in folders as images of frames of the bubble formation and text files with all the measured parameters to be processed and analyzed. The first step of processing the raw data is to upload the data onto the Fermilab server which contains all the processing and analysis codes. Although this step is usually done automatically by a weekly scheduled sync program with the local DAQ server, it had to be done manually due to a failure in the hardware. All beam events and background events were uploaded.

In the raw data, each event contains a slowDAQ log file that records the state of the detector such as the temperatures and pressures every 5 ms. Although the raw information can be useful for certain parts of the analysis, for the most part, a processed version that compiles all the useful information of each event into a single line is used. The processing scripts developed for previous PICO-0.1 calibrations used for not only PICO-0.1 but all the calibration chambers within the collaboration is used to compile all the events from both runs. Also, the data goes through an image analysis script that looks at the images from each event to come up with important information such as bubble multiplicity. Events such as Figure 6.5 would be tagged by the script to have more than one bubble. Without this program, the other reliable way would be to manually handscan every event.

6.10. Data Analysis

Once all the data is processed on the servers, the analysis of the data can begin. The analysis aims to cut all the bad events from the data using conditions for both the run and background data and provide results in the form of a binned graph. The analysis is done on MATLAB and the base code is written by Mathieu Laurin and modified for this run. An additional script was written to retrieve the livetime of the events. Since one of the problems that was encountered during the data taking was the desynchronization of the time between the beam start and the event livetime, the script took that into consideration and provided the proper livetime for all events.

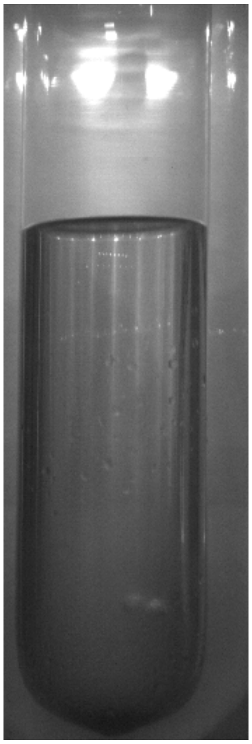

Fig. 6.5. Picture from one of the two cameras of a PICO-0.1 bubble event with more than one bubble. (Bottom of the jar)

6.10.1. Analysis Cuts

The first cut on the data run is the livetime cut. By imposing that the livetime of the event is greater than the time it takes for the beam to start, any early triggers that are clearly background events are removed. Second, a cut is imposed on the type of trigger each event is: all non-camera triggers are removed. Normally, bubble events are detected and triggered by the cameras. However, when there are instabilities inside the detector, such as abnormal pressures, the DAQ can trigger and create an event even though there are no bubbles. Lastly, any events that do not have exactly one bubble are discarded. This is tagged by the processing and multiple bubbles are most likely caused by a neutron interaction rather than the interaction of interest.

6.10.2. Event Binning

Once the dataset goes through all the cuts, the events are separated into bins matching their thresholds. For each pressure listed in Table 6.6 and 6.7, a bin is created accepting any event that falls within 2 PSIA of each pressure and falls within 1°C of the set temperature. For example, an event that has an average pressure of 30.5 PSIA and a temperature of 14°C would fall into the 30 PSIA bin, this is because of the pressure set on the DAQ is not perfectly exact and can slightly fluctuate during an expansion especially at lower pressures. Any events that do not belong in any bins are discarded. The number of events, background events, livetimes, and background livetimes are listed with its associated pressure and threshold in Table 6.6 for the first run and Table 6.7 for the second run. For the second run, extra weighting was given to the 30 and 35 PSIA pressures to have more statistics in that region.

6.10.3. Analysis Summary

Table 6.8 summarizes and compiles the data from both runs. The number of BGO background gammas for the first run is noticeably lower than the one of the second run, which is most likely caused by a shift in the energy window during the background data acquisition. Due to this issue, the analysis and discussion will focus on the second run.

Pressure (PSIA)	Threshold (keV)	Events	Bkg Events	Livetime (s)	Bkg Livetime (s)
25	2.6	116	133	1674	17458
30	3.2	117	84	1625	18796
35	3.9	107	81	1791	18710
40	5.0	100	62	1789	18838
45	6.4	105	80	1686	19493
50	8.7	102	56	1820	18677
70	48.8	80	31	2840	18689

Tab. 6.6. A summary of the pressures, thresholds, number of events, number of background events, livetimes and background livetimes for the first run (August).

6.11. Background Subtraction

The expected backgrounds listed in 6.4 can now be subtracted from the event data. The first background is the background contribution of ambient interactions. These were backgrounds measured when the gamma production was halted and are listed alongside the

Pressure (PSIA)	Threshold (keV)	Events	Bkg Events	Livetime (s)	Bkg Livetime (s)
30	3.2	245	441	4621	93152
35	3.9	245	395	4294	94217
40	5.0	155	218	2646	59344
50	8.7	135	171	2695	59352
55	12.1	129	136	2842	58606
60	17.8	113	138	3235	58677

Tab. 6.7. A summary of the pressures, thresholds, number of events, number of background events, livetimes and background livetimes for the first run (November).

	Run 1	Run 2
Total Livetime (s)	13230	20300
Total Background Livetime (s)	130661	423348
Total Number of Events	727	1022
Total Number of Background Events	529	1499
Total Number of BGO Gamma Events	172666	161982
Total Number of BGO Background Gamma Events	85	30282
Average Time per event (s)	18.2	19.9
Average Time per background event (s)	247	283

Tab. 6.8. Summary of the results from both runs after the analysis.

run results in the previous tables. This background is subtracted after being normalized over its livetime using the following equation:

$$\#\text{ of Events} - \#\text{ of Background Events} \times \frac{\text{Event Livetime}}{\text{Background Livetime}} \tag{6.11.1}$$

The same process is repeated for the BGO gammas so the results can be normalized. The normalized data set was obtained by dividing the total number of events by the total number of BGO gammas for each bin.

The second background to take into account is the alpha background. This is done by subtracting the nucleation probability of the highest threshold under the assumption that events at that threshold are mostly due to alpha interactions. From Table 6.5 and Table 6.1, it was shown that the expected recoil from both ^{12}C and ^{19}F does not surpass 10 keV. As a result, the gamma nucleation probability from the 12.1 keV threshold data was subtracted from the gamma nucleation probabilities of lower thresholds.

The third background is the dissociation of deuterium due to the water in the bath. A 1g deuterated styrene sample, containing much more deuterium than the amount expected in the bath, was placed near the active fluid and 100 events were recorded at the same run conditions for run 2. Doing the same analysis for these events showed that the event rate (second per event) did not significantly change and was still within the statistical error for all pressures that were measured. This leads to the fair assumption that the deuterium background contribution of the water in the bath is negligible.

After the background corrections listed above, the normalized gamma nucleation probability of a nuclear coherent photon recoil onto a C_3F_8 nuclei in the PICO-0.1 bubble chamber has been plotted in Figure 6.6.

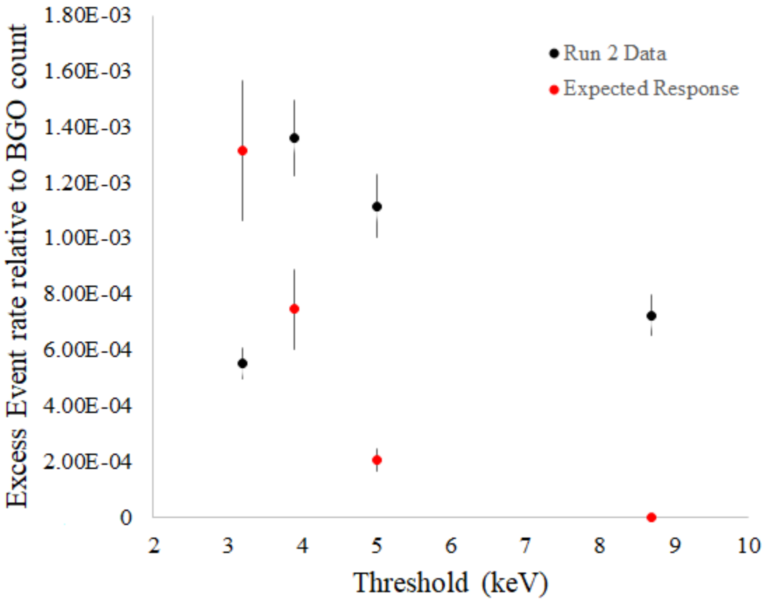

Fig. 6.6. Normalized gamma nucleation probability as a function of detector threshold of the Run 2 Data (Black) and the expected response from the theoretical coherent photon scattering interaction (Red).

Although the data from the second run was within an order of magnitude of the expected response, the event rate of the nuclear Thomson scattering was too small compared to the beam related backgrounds. Thus, the claim that this measurement was able to record the nuclear recoil of a photon cannot be made. A quick calculation indicates that out of the 1022 events recorded for a total livetime of 2.03×10^4 s, up to 1.6 events would be due to nuclear Thomson scattering. Furthermore, this estimation is an upper limit that assumes that most of the data is taken at the 30-40 PSIA thresholds. Although the conclusion of this analysis was not able to provide solid results, the method presented can be used as a basis and improved on for any future attempt at measuring this interaction.

The main limitation of this measurement was the background event rate when increasing the particle accelerator beam current. Since the beam current is directly proportional to the expected event rate, using another photon production reaction with lower energy branches could significantly reduce beam background events in PICO-0.1 and allow for a higher beam current. Another improvement would be to be able to efficiently take significantly more data. Due to the current state of the PICO-0.1 DAQ server, manually uploading all the event files from the local computer and processing them takes significantly more time than usual. An automated process would allow much more data-taking and provide much better statistics on the measurement.

Conclusion

The use of superheated liquid detectors for direct dark matter detection has improved over the years. PICASSO developed an excellent alpha discrimination technique and currently still holds exceptional limits for the spin-dependent sector while COUPP developed the bubble chamber design still currently used in PICO experiments. With PICO-40L fully built and under tests, a new era for this kind of technology begins. Fully understanding the limitations and the possible problems of this new "right-side up" design will be crucial to the development of PICO-500.

Even though future detectors such as PICO-500 will become more and more sensitive to nuclear recoils, the window to discover dark matter becomes smaller and smaller since the neutrino floor will soon become a dominant background. Each experiment will have to either discriminate this background or attempt to shield it.

Although the work in this thesis was not able to properly measure the nuclear Thomson scattering, which will prove to be a significant background in future sub-keV threshold detectors, this attempt can be used as a baseline for future measurements using PICO-0.1. By implementing the suggested improvements in Chapter 6, such as using a gamma source with lower energies and taking a significantly larger amount of data, better results can show whether or not PICO-0.1 is reliably able to measure this background.

References

---

[1] M. G. Aartsen and et al. Search for annihilating dark matter in the sun with 3 years of icecube data. *The European Physical Journal C*, 77(3), Mar 2017.

[2] A.H. Abdelhameed and et al. First results from the cresst-iii low-mass dark matter program. *Physical Review D*, 100(10), Nov 2019.

[3] Govinda Adhikari and et al. An experiment to search for dark-matter interactions using sodium iodide detectors. *Nature*, 564(7734):83–86, 2018.

[4] R. Agnese and et al. Low-mass dark matter search with cdmslite. *Physical Review D*, 97(2), Jan 2018.

[5] R. Agnese and et al. Results from the super cryogenic dark matter search experiment at soudan. *Physical Review Letters*, 120(6), Feb 2018.

[6] R. Agnese and et al. Search for low-mass dark matter with cdmslite using a profile likelihood fit. *Physical Review D*, 99(6), Mar 2019.

[7] R. Ajaj and et al. Search for dark matter with a 231-day exposure of liquid argon using deap-3600 at snolab. *Physical Review D*, 100(2), Jul 2019.

[8] D. S. Akerib et al. Results from a search for dark matter in LUX with 332 live days of exposure. *ArXiv e-prints*, August 2016.

[9] D.S. Akerib and et al. Limits on spin-dependent wimp-nucleon cross section obtained from the complete lux exposure. *Physical Review Letters*, 118(25), Jun 2017.

[10] D. Akimov and et al. Coherent 2018 at the spallation neutron source, 2018.

[11] D.Yu. Akimov and et al. Wimp-nucleon cross-section results from the second science run of zeplin-iii. *Physics Letters B*, 709(1-2):14 – 20, 2012.

[12] C. Amole and et al. Dark matter search results from the pico-2l c_3f_8 bubble chamber. *Physical Review Letters*, 114:231302, Jun 2015.

[13] C. Amole and et al. Dark matter search results from the pico-60 cf_3I bubble chamber. *Phys. Rev. D*, 93:052014, Mar 2016.

[14] C. Amole and et al. Improved dark matter search results from pico-2l run 2. *Phys. Rev. D*, 93:061101, Mar 2016.

[15] C. Amole and et al. Dark matter search results from the PICO$-$60 c_3f_8 bubble chamber. *Phys. Rev. Lett.*, 118:251301, Jun 2017.

[16] C. Amole and et al. Dark Matter Search Results from the Complete Exposure of the PICO-60 C$_3$F$_8$ Bubble Chamber. *arXiv e-prints*, page arXiv:1902.04031, Feb 2019.

[17] C. Amole and et al. Data-driven modeling of electron recoil nucleation in pico c3f8 bubble chambers. *Physical Review D*, 100(8), Oct 2019.

[18] E. Aprile and et al. Xenon100 dark matter results from a combination of 477 live days. *Physical Review D*, 94(12), Dec 2016.

[19] E. Aprile et al. Light dark matter search with ionization signals in xenon1t. 2019.

[20] E. Behnke and et al. First dark matter search results from a 4-kg $\mathrm{cf}_3\mathbf{I}$ bubble chamber operated in a deep underground site. *Phys. Rev. D*, 86:052001, Sep 2012.

[21] E. Behnke and et al. First dark matter search results from a 4-kgcf3ibubble chamber operated in a deep underground site. *Physical Review D*, 86(5), Sep 2012.

[22] E. Behnke and et al. Final results of the PICASSO dark matter search experiment. *Astropart. Phys.*, 90:85–92, apr 2017.

[23] Coursey J.S. Zucker M.A. Berger, M.J. and J. Chang. Estar, pstar, and astar: Computer programs for calculating stopping-power and range tables for electrons, protons, and helium ions (version 1.2.3), 2005.

[24] U. Chowdhury and T. Hillier. Cleaning pico-40. *COUPP internal document*, (2945), 2017.

[25] Xiangyi Cui and et al. Dark matter results from 54-ton-day exposure of pandax-ii experiment. *Physical Review Letters*, 119(18), Oct 2017.

[26] Fustin A. Drew. First dark matter limits from the coupp 4 kg bubble chamber at a deep underground site. *University of Chicago PhD Thesis*, 2012.

[27] M. Felizardo and et al. Final analysis and results of the phase ii simple dark matter search. *Physical Review Letters*, 108(20), May 2012.

[28] Daniel Z. Freedman. Coherent effects of a weak neutral current. *Phys. Rev. D*, 9:1389–1392, Mar 1974.

[29] Changbo Fu and et al. Spin-dependent weakly-interacting-massive-particle–nucleon cross section limits from first data of pandax-ii experiment. *Physical Review Letters*, 118(7), Feb 2017.

[30] Donald A. Glaser. Some effects of ionizing radiation on the formation of bubbles in liquids. *Phys. Rev.*, 87:665–665, Aug 1952.

[31] J. H. Hubbell and S. M. Seltzer. Tables of x-ray mass attenuation coefficients and mass energy-absorption coefficients from 1 kev to 20 mev for elements z = 1 to 92 and 48 additional substances of dosimetric interest, 2004.

[32] M. Kuźniak and et al. Deap-3600 dark matter search. *Nuclear and Particle Physics Proceedings*, 273-275:340–346, Apr 2016.

[33] M. Laurin. Master pico-40l drawing repository. *COUPP internal document*, (3648), 2018.

[34] B. Lehnert. Backgrounds in the deap-3600 dark matter experiment, 2018.

[35] J. D. Lewin and P. F. Smith. Review of mathematics, numerical factors, and corrections for dark matter experiments based on elastic nuclear recoil. *Astroparticle Physics*, 6(1):87 – 112, 1996.

[36] M. Mitchell. Engauge digitizer, 2019.

[37] University of Sheffield. Dark matter wimp wind figure, 2020.

[38] Ciaran A. J. O'Hare and et al. Velocity substructure from gaia and direct searches for dark matter. *Phys. Rev. D*, 101:023006, Jan 2020.

[39] Arthur Plante. Searching for dark matter with superheated liquid detectors. *University of Montreal PhD Thesis*, 2019.

[40] Alan E. Robinson. Dark matter limits from a 2l c3f8 filled bubble chamber. *University of Chicago PhD Thesis*, 2015.

[41] Alan E. Robinson. Coherent photon scattering background in sub- gev/c2 direct dark matter searches [phys. rev. d 95 , 021301(r) (2017)]. *Physical Review D*, 95(6), Mar 2017.

[42] W. K. Jr.; Thonnard N. Rubin, V. C.; Ford. Rotational properties of 21 sc galaxies with a large range of luminosities and radii, from ngc 4605 (r=4kpc) to ugc 2885 (r=122kpc). *Astrophysical Journal*, 238(1):471 – 487, 1980.

[43] DING S. and et al. The characteristics of 67 mev photons emitted in the ^{19}f(p,$\alpha\gamma$)^{16}o reactions.

[44] Tarek Saab and Enectali Figueroa. Wimp limit plotter.

[45] SNOLAB. SNOLAB user handbook, 2006.

[46] K. Spyrou and et al. Cross section and resonance strengths of the ^{19}f(p,|aγ)^{16}o reaction in the energy range e(p) = 0.8 - 3.6 mev. *Zeitschrift fuer Physik A, Hadrons and Nuclei*, 357:283, 1997.

[47] Frédéric Tardif. Direct detection of dark matter with the pico experiment and the pico-0.1 calibration chamber. *University of Montreal Master Thesis*, 2018.

[48] A. N. Taylor, S. Dye, T. J. Broadhurst, N. Benitez, and E. van Kampen. Gravitational lens magnification and the mass of abell 1689. *The Astrophysical Journal*, 501(2):539–553, Jul 1998.

[49] D. B. Tridapalli and et al. 19f (p, alpha gamma) 16o reaction: Hpge detector response function and gamma-ray relative yields, 2007.

[50] C.T.R. Wilson. On an Expansion Apparatus for Making Visible the Tracks of Ionising Particles in Gases and Some Results Obtained by Its Use. *Proc. Roy. Soc. Lond. A*, A87(595):277–292, 1912.

[51] Yu-Cheng Wu and et al. Measurement of cosmic ray flux in the china JinPing underground laboratory. *Chinese Physics C*, 37(8):086001, aug 2013.

[52] F. Zwicky. Die rotverschiebung von extragalaktischen nebeln. *Helvetica Physica Acta*, 6(1):110 – 127, 1933.